Eur. Phys. J. C (2014) 74:3108
DOI 10.1140/epjc/s10052-014-3108-8

THE EUROPEAN PHYSICAL JOURNAL C

Regular Article - Experimental Physics

Neutral pion production at midrapidity in pp and Pb–Pb collisions at $\sqrt{s_{\rm NN}} = 2.76$ TeV

The ALICE Collaboration[*]

CERN, 1211 Geneva 23, Switzerland

Received: 16 May 2014 / Accepted: 30 September 2014 / Published online: 16 October 2014

Abstract Invariant yields of neutral pions at midrapidity in the transverse momentum range $0.6 < p_{\rm T} < 12$ GeV/c measured in Pb–Pb collisions at $\sqrt{s_{\rm NN}} = 2.76$ TeV are presented for six centrality classes. The pp reference spectrum was measured in the range $0.4 < p_{\rm T} < 10$ GeV/c at the same center-of-mass energy. The nuclear modification factor, $R_{\rm AA}$, shows a suppression of neutral pions in central Pb–Pb collisions by a factor of up to about 8−10 for $5 \lesssim p_{\rm T} \lesssim 7$ GeV/c. The presented measurements are compared with results at lower center-of-mass energies and with theoretical calculations.

1 Introduction

Quantum chromodynamics (QCD) predicts a transition from hadronic matter to a state of deconfined quarks and gluons, i.e., to the quark-gluon plasma (QGP), at a temperature of $T_c \approx 150-160$ MeV at vanishing net baryon number [1,2]. Energy densities created in Pb–Pb collisions at the LHC are estimated to be sufficiently large to reach this state [3,4]. At low transverse momenta (roughly $p_{\rm T} \lesssim 3$ GeV/c) it is expected that pressure gradients in the QGP produced in an ultrarelativistic collision of two nuclei give rise to a collective, outward-directed velocity profile, resulting in a characteristic modification of hadron spectra [5]. At sufficiently large $p_{\rm T}$ ($\gtrsim 3-8$ GeV/c), hadrons in pp and Pb–Pb collisions originate from hard scattering as products of jet fragmentation. Hard-scattered quarks and gluons, produced in the initial stage of the heavy-ion collision, must traverse the QGP that is produced around them and lose energy in the process through interactions with that medium. This phenomenon ("jet quenching") leads to a modification of hadron yields at high $p_{\rm T}$ [6,7]. By studying observables related to jet quenching one would like to better understand the mechanism of parton energy loss and to use hard probes as a tool to characterize the QGP.

The modification of the hadron yields for different $p_{\rm T}$ intervals in heavy-ion (A–A) collisions with respect to pp collisions can be quantified with the nuclear modification factor

$$R_{\rm AA}(p_{\rm T}) = \frac{{\rm d}^2N/{\rm d}p_{\rm T}{\rm d}y|_{\rm AA}}{\langle T_{\rm AA}\rangle \times {\rm d}^2\sigma/{\rm d}p_{\rm T}{\rm d}y|_{\rm pp}} \quad (1)$$

where the nuclear overlap function $\langle T_{\rm AA}\rangle$ is related to the average number of inelastic nucleon-nucleon collisions as $\langle T_{\rm AA}\rangle = \langle N_{\rm coll}\rangle/\sigma_{\rm inel}^{\rm pp}$. In the factorization approach of a perturbative QCD calculation of particle production from hard scattering, the overlap function $T_{\rm AA}$ can be interpreted as the increase of the parton flux in going from pp to A–A collisions. Without nuclear effects, $R_{\rm AA}$ will be unity in the hard scattering regime.

Parton energy loss depends on a number of factors including the transport properties of the medium and its space-time evolution, the initial parton energy, and the parton type [8–12]. The nuclear modification factor, $R_{\rm AA}$, is also affected by the slope of the initial parton transverse momentum spectrum prior to any interaction with the medium and by initial-state effects like the modifications of the parton distributions in nuclei. An important constraint for modeling these effects comes from the study of p–A collisions [13], but also from the study of A–A collisions at different center-of-mass energies ($\sqrt{s_{\rm NN}}$) and different centralities. For instance, the increase in $\sqrt{s_{\rm NN}}$ from RHIC to LHC energies by about a factor 14 results in larger initial energy densities and less steeply falling initial parton spectra [14]. Moreover, at the LHC, pions with $p_{\rm T} \lesssim 50$ GeV/c are dominantly produced in the fragmentation of gluons [15], whereas the contribution from quark fragmentation in the same $p_{\rm T}$ region is much larger and more strongly varying with $p_{\rm T}$ at RHIC [16]. Therefore, the pion suppression results at the LHC will be dominated by gluon energy loss, and simpler to interpret than the results from RHIC. Compared to measurements of the $R_{\rm AA}$ for inclusive charged hadrons, differences between the baryon and meson $R_{\rm AA}$ provide additional information on the parton energy loss mechanism and/or on hadronization in A–A collisions

[*] e-mail: alice-publications@cern.ch

[17,18]. Experimentally, neutral pions are ideally suited for this as they can be cleanly identified (on a statistical basis) via the decay $\pi^0 \to \gamma\gamma$.

The suppression of neutral pions and charged hadrons at large transverse momentum [19–23] and the disappearance of azimuthal back-to-back correlations of charged hadrons in central Au–Au collision at RHIC [24,25] (see also [26–29]) were interpreted in terms of parton energy loss in hot QCD matter. Neutral pions in central Au–Au collisions at $\sqrt{s_{\rm NN}} = 200$ GeV were found to be suppressed by a factor of 4−5 for $p_{\rm T} \gtrsim 4$ GeV/c [30,31]. The rather weak dependence of $R_{\rm AA}$ on $p_{\rm T}$ was described by a large number of jet quenching models [32]. The $\sqrt{s_{\rm NN}}$ and system size dependence was studied in Cu-Cu collisions at $\sqrt{s_{\rm NN}} = 19.4, 62.4$, and 200 GeV [33] and in Au–Au collisions at $\sqrt{s_{\rm NN}} = 39$, 62.4, and 200 GeV [22,34]. In central Cu-Cu collisions the onset of $R_{\rm AA} < 1$ was found to occur between $\sqrt{s_{\rm NN}} = 19.4$ and 62.4 GeV. For unidentified charged hadrons in central Pb–Pb collisions at the LHC, $R_{\rm AA}$ was found to increase from $R_{\rm AA} < 0.2$ at $p_{\rm T} \approx 7$ GeV/c to $R_{\rm AA} \approx 0.5$ for $p_{\rm T} \gtrsim 50$ GeV/c, in line with a decrease of the relative energy loss with increasing parton $p_{\rm T}$ [35–37].

The dependence of the neutral pion $R_{\rm AA}$ on $\sqrt{s_{\rm NN}}$ and $p_{\rm T}$ in Au–Au collisions at RHIC energies for $2 \lesssim p_{\rm T} \lesssim 7$ GeV/c is not fully reproduced by jet quenching calculations in the GLV framework which is based on perturbative QCD [34,38,39]. This may indicate that, especially for this intermediate $p_{\rm T}$ range, jet quenching calculations do not yet fully capture the relevant physics processes. With the large increase in $\sqrt{s_{\rm NN}}$ the measurement of $R_{\rm AA}$ at the LHC provides a large lever arm to further constrain parton energy loss models. Phenomena affecting pion production in the $p_{\rm T}$ range $0.6 < p_{\rm T} < 12$ GeV/c of this measurement include collective radial flow at low $p_{\rm T}$ and parton energy loss at high $p_{\rm T}$. The data are therefore well suited to test models aiming at a description of particle production over the full transverse momentum range, including the potentially complicated interplay between jets and the evolving medium.

2 Detector description

Neutral pions were reconstructed via the two-photon decay channel $\pi^0 \to \gamma\gamma$ which has a branching ratio of 98.8 % [40]. Two independent methods of photon detection were employed: with the photon spectrometer (PHOS) which is an electromagnetic calorimeter [41], and with photon conversions measured in the central tracking system using the inner tracking system (ITS) [42] and the time projection chamber (TPC) [43]. In the latter method, referred to as photon conversion method (PCM), conversions out to the middle of the TPC were reconstructed (radial distance $R \approx 180$ cm). The material in this range amounts to (11.4 ± 0.5) % of a radiation length X_0 for $|\eta| < 0.9$ corresponding to a plateau value of the photon conversion probability of (8.6 ± 0.4) %. The measurement of neutral pions with two independent methods with different systematics and with momentum resolutions having opposite dependence on momentum provides a valuable check of the systematic uncertainties and facilitates the measurements of neutral pions in a wide momentum range with small systematic uncertainty.

PHOS consists of three modules installed at a distance of 4.6 m from the interaction point. PHOS subtends $260° < \varphi < 320°$ in azimuth and $|\eta| < 0.13$ in pseudorapidity. Each module has 3584 detection channels in a matrix of 64×56 cells made of lead tungstate ($PbWO_4$) crystals each of size $2.2 \times 2.2 \times 18\,{\rm cm}^3$. The transverse dimensions of the cells are slightly larger than the $PbWO_4$ Molière radius of 2 cm. The signals from the cells are measured by avalanche photodiodes with a low-noise charge-sensitive preamplifier. In order to increase the light yield and thus to improve energy resolution, PHOS crystals are cooled down to a temperature of −25 °C. The PHOS cells were calibrated in pp collisions by equalizing the π^0 peak position for all cell combinations registering a hit by a decay photon.

The inner tracking system (ITS) [44] consists of two layers of silicon pixel detectors (SPD) positioned at a radial distance of 3.9 and 7.6 cm, two layers of silicon drift detectors (SDD) at 15.0 and 23.9 cm, and two layers of silicon strip detectors (SSD) at 38.0 and 43.0 cm. The two SPD layers cover a pseudorapidity range of $|\eta| < 2$ and $|\eta| < 1.4$, respectively. The SDD and the SSD subtend $|\eta| < 0.9$ and $|\eta| < 1.0$, respectively.

The time projection chamber (TPC) [43] is a large (85 m^3) cylindrical drift detector filled with a $Ne/CO_2/N_2$ (85.7/9.5/4.8 %) gas mixture. It covers a pseudorapidity range of $|\eta| < 0.9$ over the full azimuthal angle for the maximum track length of 159 reconstructed space points. With the magnetic field of $B = 0.5$ T, electron and positron tracks were reconstructed down to transverse momenta of about 50 MeV/c. In addition, the TPC provides particle identification via the measurement of the specific energy loss (dE/dx) with a resolution of 5.5 % [43]. The ITS and the TPC were aligned with respect to each other to a precision better than 100 μm using tracks from cosmic rays and proton–proton collisions [42].

Two forward scintillator hodoscopes (VZERO-A and VZERO-C) [45] subtending $2.8 < \eta < 5.1$ and $-3.7 < \eta < -1.7$, respectively, were used in the minimum bias trigger in the pp and in the Pb–Pb run. The sum of the amplitudes of VZERO-A and VZERO-C served as a measure of centrality in Pb–Pb collisions [46]. Spectator (non-interacting) protons and neutrons were measured with zero degree calorimeters (ZDCs), located close to the beam pipe, 114 m away from the interaction point on either side of the ALICE detector [44].

3 Data processing

3.1 Event selection

The pp sample at $\sqrt{s} = 2.76$ TeV was collected in the 2011 LHC run. The minimum bias trigger (MB_{OR}) in the pp run required a hit in either VZERO hodoscope or a hit in the SPD. Based on a van der Meer scan the cross section for inelastic pp collisions was determined to be $\sigma_{inel} = (62.8^{+2.4}_{-4.0} \pm 1.2)$ mb and the MB_{OR} trigger had an efficiency of $\sigma_{MB_{OR}}/\sigma_{inel} = 0.881^{+0.059}_{-0.035}$ [47]. The results were obtained from samples of 34.7×10^6 (PHOS) and 58×10^6 (PCM) minimum bias pp collisions corresponding to an integrated luminosity $\mathcal{L}_{int} = 0.63\,\text{nb}^{-1}$ and $\mathcal{L}_{int} = 1.05\,\text{nb}^{-1}$, respectively. PHOS and the central tracking detectors used in the PCM were in different readout partitions of the ALICE experiment which resulted in the different integrated luminosities.

The Pb–Pb data at $\sqrt{s_{NN}} = 2.76$ TeV were recorded in the 2010 LHC run. At the ALICE interaction region up to 114 bunches, each containing about 7×10^7 ^{208}Pb ions, were collided. The rate of hadronic interactions was about 100 Hz, corresponding to a luminosity of about $1.3 \times 10^{25}\,\text{cm}^{-2}\text{s}^{-1}$. The detector readout was triggered by the LHC bunch-crossing signal and a minimum bias interaction trigger based on trigger signals from VZERO-A, VZERO-C, and SPD [46]. The efficiency for triggering on a hadronic Pb–Pb collision ranged between 98.4 and 99.7 %, depending on the minimum bias trigger configuration. For the centrality range 0-80 % studied in the Pb–Pb analyses 16.1×10^6 events in the PHOS analysis and 13.2×10^6 events in the PCM analysis passed the offline event selection.

In both pp and Pb–Pb analyses, the event selection was based on VZERO timing information and on the correlation between TPC tracks and hits in the SPD to reject background events coming from parasitic beam interactions. In addition, an energy deposit in the ZDCs of at least three standard deviations above the single-neutron peak was required for Pb–Pb collisions to further suppress electromagnetic interactions [46]. Only events with a reconstructed vertex in $|z_{vtx}| < 10$ cm with respect to the nominal interaction vertex position along the beam direction were used.

3.2 Neutral pion reconstruction

The PHOS and PCM analyses presented here are based on methods previously used in pp collisions at $\sqrt{s} = 0.9$ and 7 TeV [48]. Neutral pions were reconstructed using the $\pi^0 \to \gamma\gamma$ decay channel either with both photon candidates detected in PHOS or both photons converted into e^+e^- pairs and reconstructed in the central tracking system. For the photon measurement with PHOS adjacent lead tungstate cells with energy signals above a threshold (12 MeV) were grouped into clusters [49]. The energies of the cells in a cluster were summed up to determine the photon energy. The selection of the photon candidates in PHOS was different for pp and Pb–Pb collisions due to the large difference in detector occupancy. For pp collisions cluster overlap is negligible and combinatorial background small. Therefore, only relatively loose photon identification cuts on the cluster parameters were used in order to maximize the π^0 reconstruction efficiency: the cluster energy for pp collisions was required to be above the minimum ionizing energy $E_{cluster} > 0.3$ GeV and the number of cells in a cluster was required to be greater than two to reduce the contribution of hadronic clusters. In the case of the most central Pb–Pb collisions about 80 clusters are reconstructed in PHOS, resulting in an occupancy of up to 1/5 of the 10,752 PHOS cells. This leads to a sizable probability of cluster overlap and to a high combinatorial background in the two-cluster invariant mass spectra. A local cluster maximum was defined as a cell with a signal at least 30 MeV higher than the signal in each surrounding cell. A cluster with more than one local maximum was unfolded to several contributing clusters [49]. As the lateral width of showers resulting from hadrons is typically larger than the one of photon showers, non-photonic background was reduced by a p_T dependent shower shape cut. This cut is based on the eigenvalues λ_0, λ_1 of the covariance matrix built from the cell coordinates and weights $w_i = \max[0, w_0 + \log(E_i/E_{cluster})]$, $w_0 = 4.5$ where E_i is the energy measured in cell i. In the Pb–Pb case only cells with a distance to the cluster center of $R_{disp} = 4.5$ cm were used in the dispersion calculation. A 2D p_T-dependent cut in the λ_0-λ_1 plane was tuned to have an efficiency of $\sim$0.95 using pp data. In addition, clusters associated with a charged particle were rejected by application of a cut on the minimum distance from a PHOS cluster to the extrapolation of reconstructed tracks to the PHOS surface [49]. This distance cut depended on track momentum and was tuned by using real data to minimize false rejection of photon clusters. The corresponding loss of the π^0 yield was about 1 % in pp collisions (independent of p_T). In Pb–Pb collisions the π^0 inefficiency due to the charged particle rejection is about 1 % in peripheral and increases to about 7 % in central Pb–Pb collisions. In addition, to reduce the effect of cluster overlap, the cluster energy was taken as the *core energy* of the cluster, summing over cells with centers within a radius $R_{core} = 3.5$ cm of the cluster center of gravity, rather than summing over all cells of the cluster. By using the core energy, the centrality dependence of the width and position of the π^0 peak is reduced, due to a reduction of overlap effects. The use of the core energy leads to an additional non-linearity due to energy leakage outside R_{core}: the difference between full and core energy is negligible at $E_{cluster} \lesssim 1$ GeV and reaches $\sim$4 % at $E_{cluster} \sim 10$ GeV. This non-linearity, however, is well reproduced in the GEANT3 Monte Carlo simulations [50]

of the PHOS detector response (compare p_{T} dependences of peak positions in data and Monte Carlo in Fig. 2) and is corrected for in the final spectra.

PHOS is sensitive to pile-up from multiple events that occur within the 6 μs readout interval of the PHOS front-end electronics. The shortest time interval between two bunch crossings in pp collisions was 525 ns. To suppress photons produced in other bunch crossings, a cut on arrival time $|t| < 265$ ns was applied to reconstructed clusters which removed 16 % of the clusters. In the Pb–Pb collisions, the shortest time interval between bunch crossing was 500 ns, but the interaction probability per bunch crossing was much smaller than in pp collisions. To check for a contribution from other bunch crossings to the measured spectra, a timing cut was applied, and the pile-up contribution was found to be negligible in all centrality classes. Therefore, a timing cut was not applied in the final PHOS Pb–Pb analysis.

The starting point of the conversion analysis is a sample of photon candidates corresponding to track pairs reconstructed by a secondary vertex (V0) finding algorithm [49,51]. In this step, no constraints on the reconstructed invariant mass and pointing of the momentum vector to the collision vertex were applied. Both tracks of a V0 were required to contain reconstructed clusters (i.e., space points) in the TPC. V0's were accepted as photon candidates if the ratio of the number of reconstructed TPC clusters over the number of findable clusters (taking into account track length, spatial location, and momentum) was larger than 0.6 for both tracks. In order to reject K^0_s, Λ, and $\bar{\Lambda}$ decays, electron selection and pion rejection cuts were applied. V0's used as photon candidates were required to have tracks with a specific energy loss in the TPC within a band of $[-3\sigma, 5\sigma]$ around the average electron $\mathrm{d}E/\mathrm{d}x$, and of more than 3σ above the average pion $\mathrm{d}E/\mathrm{d}x$ (where the second condition was only applied for tracks with measured momenta $p > 0.4\,\mathrm{GeV/c}$). Moreover, tracks with an associated signal in the TOF detector were only accepted as photon candidates if they were consistent with the electron hypothesis within a $\pm 5\sigma$ band. A generic particle decay model based on the Kalman filter method [52] was fitted to a reconstructed V0 assuming that the particle originated from the primary vertex and had a mass $M_{V0} = 0$. Remaining contamination in the photon sample was reduced by cutting on the χ^2 of this fit. Furthermore, the transverse momentum $q_T = p_e \sin\theta_{V0,e}$ [53] of the electron, p_e, with respect to the V0 momentum was restricted to $q_T < 0.05\,\mathrm{GeV/c}$. As the photon is massless, the difference $\Delta\theta = |\theta_{e^-} - \theta_{e^+}|$ of the polar angles of the electron and the positron from a photon conversion is small and the bending of the tracks in the magnetic field only results in a difference $\Delta\varphi = |\varphi_{e^-} - \varphi_{e^+}|$ of the azimuthal angles of the two momentum vectors. Therefore, remaining random track combinations, reconstructed as a V0, were suppressed further by a cut on the ratio of $\Delta\theta$ to the total opening angle of the e^+e^- pair calculated after propagating both the electron and the positron 50 cm from the conversion point in the radial direction. In order to reject e^+e^- pairs from Dalitz decays the distance between the nominal interaction point and the reconstructed conversion point of a photon candidate had to be larger than 5 cm in radial direction. The maximum allowed radial distance for reconstructed V0's was 180 cm.

Pile-up of neutral pions coming from bunch crossings other than the triggered one also has an effect on the PCM measurement. At the level of reconstructed photons, this background is largest for photons for which both the electron and the positron were reconstructed with the TPC alone without tracking information from the ITS. These photons, which typically converted at large radii R, constitute a significant fraction of the total PCM photon sample, which is about 67 % in case of the pp analysis. This sample is affected because the TPC drift velocity of 2.7 cm/μs corresponds to a drift distance of 1.41 cm between two bunch crossings in the pp run which is a relatively short distance compared to the width of $\sigma_z \approx 5$ cm of the distribution of the primary vertex in the z direction. The distribution of the distance of closest approach in the z direction (DCA_z) of the straight line defined by the reconstructed photon momentum is wider for photons from bunch crossings other than the triggered one. The DCA_z distribution of photons which had an invariant mass in the π^0 mass range along with a second photon was measured for each p_{T} interval. Entries in the tails at large DCA_z were used to determine the background distribution and to correct the neutral pion yields for inter bunch pile-up. For the pp analysis, this was a 5−7 % correction for $p_{\mathrm{T}} \gtrsim 2\,\mathrm{GeV/c}$ and a correction of up to 15 % at lower p_{T} ($p_{\mathrm{T}} \approx 1\,\mathrm{GeV/c}$). In the Pb–Pb case the correction at low p_{T} was about 10 %, and became smaller for higher p_{T} and for more central collisions. For the 20−40 % centrality class and more central classes the pile-up contribution was negligible and no pile-up correction was applied. In the PCM as well as in the PHOS analysis, events for which two or more pp or Pb–Pb interactions occurred in the same bunch crossing were rejected based on the number of primary vertices reconstructed with the SPD [49] which has an integration time of less than 200 ns.

In the PHOS as well as in the PCM analysis, the neutral pion yield was extracted from a peak above a combinatorial background in the two-photon invariant mass spectrum. Examples of invariant mass spectra, in the π^0 mass region, are shown in Fig. 1 for selected p_{T} bins for pp collisions, and peripheral and central Pb–Pb collisions. The combinatorial background was determined by mixing photon candidates from different events. In the PCM measurement the combinatorial background was reduced by cutting on the energy asymmetry $\alpha = |E_{\gamma_1} - E_{\gamma_2}|/(E_{\gamma_1} + E_{\gamma_2})$, where $\alpha < 0.65$ was required for the central classes (0−5, 5−10, 10−20, 20−40 %) and $\alpha < 0.8$ for the two peripheral classes

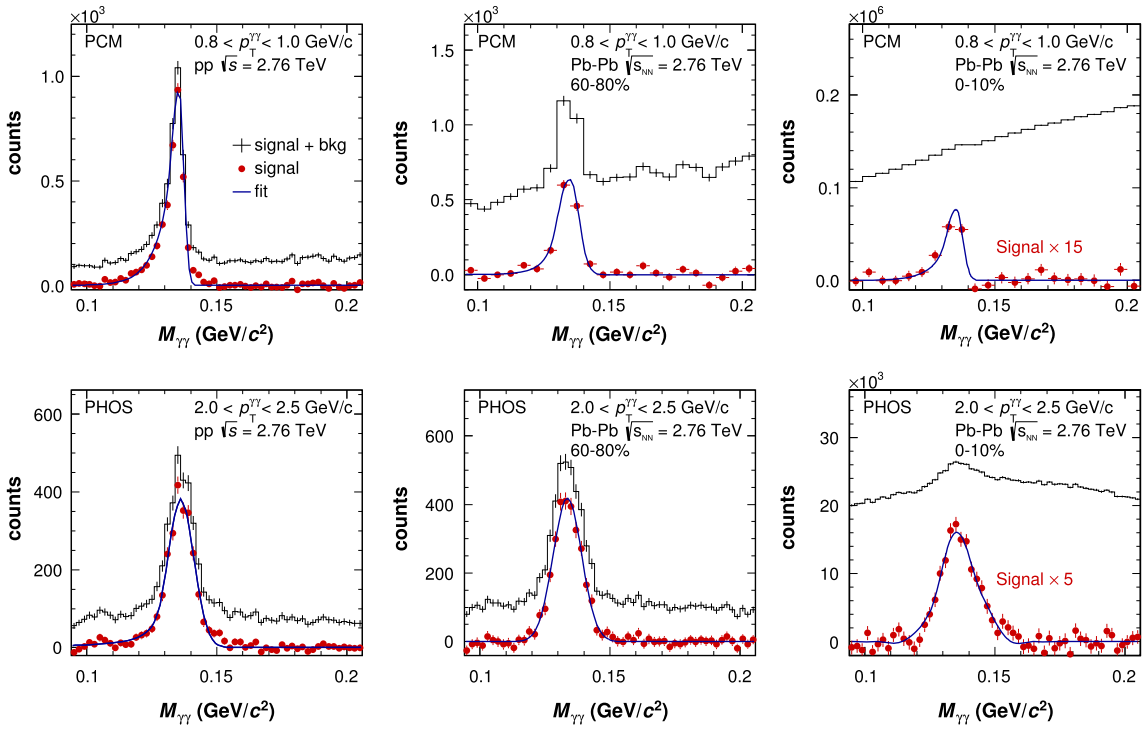

Fig. 1 (Color online) Invariant mass spectra in selected p_T slices for PCM (*upper row*) and PHOS (*lower row*) in the π^0 mass region for pp (*left column*), 60−80 % (*middle column*) and 0−10 % (*right column*) Pb–Pb collisions. The *histogram* and the *filled points* show the data before and after background subtraction, respectively. For the 0−10 % class the invariant mass distributions after background subtraction were scaled by a factor 15 and 5 for PCM and PHOS, respectively, for better visibility of the peak. The positions and widths of the π^0 peaks were determined from the fits, shown as *blue curves*, to the invariant mass spectra after background subtraction

(40−60, 60−80 %). In both analyses the mixed-event background distributions were normalized to the right and left sides of the π^0 peak. A residual correlated background was taken into account using a linear or second order polynomial fit. The π^0 peak parameters were obtained by fitting a function, Gaussian or a Crystal Ball function [54] in the PHOS case or a Gaussian combined with an exponential low mass tail to account for bremsstrahlung [55] in the PCM case, to the background-subtracted invariant mass distribution, see Fig. 1. The Crystal Ball function was used in the PHOS analysis of pp data. A Gaussian was used alternatively to determine systematic uncertainties of the peak parameters. In the Pb–Pb case with worse resolution and smaller signal/background ratios, the difference between Crystal Ball and Gaussian fits disappeared and only the latter were used in the PHOS analysis. In the case of PHOS the number of reconstructed π^0's was obtained in each p_T bin by integrating the background subtracted peak within 3 standard deviations around the mean value of the π^0 peak position. In the PCM analysis, the integration window was chosen to be asymmetric (m_{π^0} − 0.035 GeV/c^2, m_{π^0} + 0.010 GeV/c^2) to take into account the left side tail of the π^0 peak due to bremsstrahlung energy loss of electrons and positrons from photon conversions. In both analyses the normalization and integration windows were varied to estimate the related systematic uncertainties. The peak positions and widths from the two analyses are compared to GEANT3 Monte Carlo simulations in Fig. 2 as a function of p_T. The input for the GEANT3 simulation came from the event generators PYTHIA 8 [56] and PHOJET [57] in the case of pp collisions (with roughly equal number of events) and from HIJING [58] in the case of Pb–Pb collisions. For the PCM analysis the full width at half maximum (FWHM) divided by $2\sqrt{2\ln 2} \approx 2.35$ is shown. Note the decrease of the measured peak position with p_T in Pb–Pb collisions for PHOS. This is due to the use of the core energy instead of the full cluster energy. At low p_T in central Pb–Pb collisions, shower overlaps can increase the cluster energy thereby resulting in peak positions above the nominal π^0 mass. A good agreement in peak position and width between data and simulation is observed in both analyses. The remaining small deviations in the case of PHOS were taken into account as a systematic uncertainty related to the global energy scale.

The correction factor $\varepsilon(p_T)$ for the PHOS detector response and the acceptance $A(p_T)$ were calculated with GEANT3 Monte Carlo simulations tuned to reproduce the detector response. The factor $\varepsilon(p_T)$ takes the loss of neutral pions due to analysis cuts, effects of the finite energy resolution and, in case of Pb–Pb collisions, effects of shower overlaps into account. The shape of the π^0 input spectrum needed

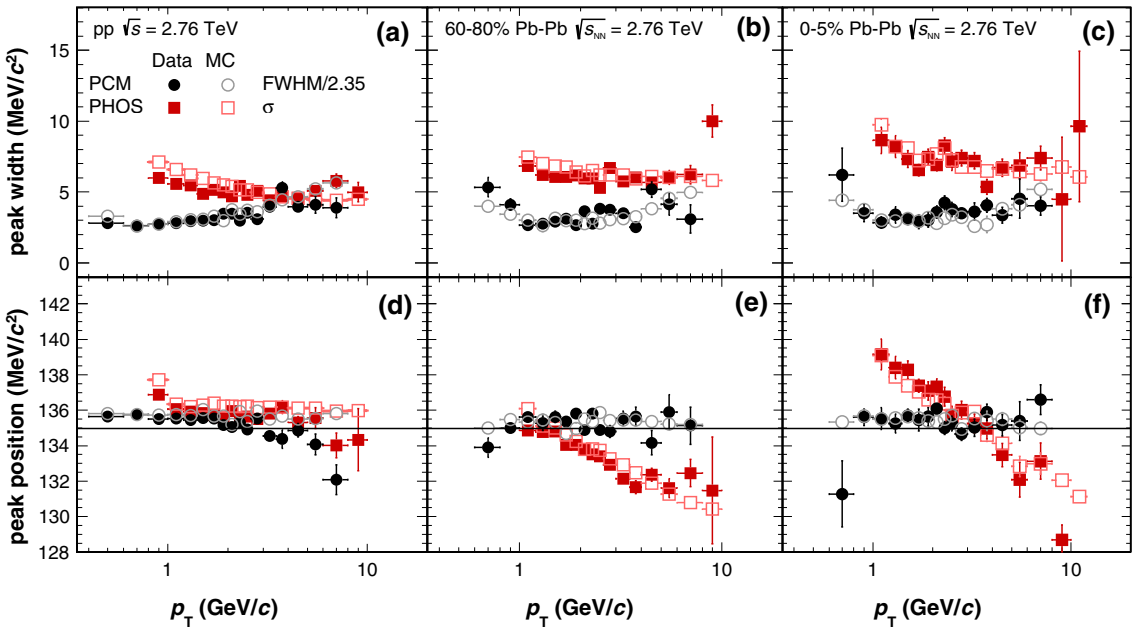

Fig. 2 (Color online) Reconstructed π^0 peak width (*upper row*) and position (*lower row*) as a function of p_T in pp collisions at $\sqrt{s}$ = 2.76 TeV (**a**, **d**), peripheral (**b**, **e**) and central (**c**, **f**) Pb–Pb collisions at $\sqrt{s_{NN}}$ = 2.76 TeV in PHOS and in the photon conversion method (PCM) compared to Monte Carlo (MC) simulations. The *horizontal line* in (**d**–**f**) indicates the nominal π^0 mass

for the calculation of $\varepsilon(p_T)$ was determined iteratively by using a fit of the corrected spectrum of a given pass as input to the next. In the case of Pb–Pb collisions the embedding technique was used in the PHOS analysis: the PHOS response to single π^0's was simulated, the simulated π^0 event was added to a real Pb–Pb event on the cell signal level, after which the standard reconstruction procedure was performed. The correction factor $\varepsilon(p_T) = (N_{rec}^{after}(p_T) - N_{rec}^{before}(p_T))/N_{sim}(p_T)$ was defined as the ratio of the difference of the number of reconstructed π^0's after and before the embedding to the number of simulated π^0's. In the pp case, the PHOS occupancy was so low that embedding was not needed and $\varepsilon(p_T)$ was obtained from the π^0 simulations alone. Both in the Pb–Pb and the pp analysis, an additional 2 % channel-by-channel decalibration was introduced to the Monte Carlo simulations, as well as an energy non-linearity observed in real data at low energies which is not reproduced by the GEANT simulations. This non-linearity is equal to 2.2 % at $p_T = 1$ GeV/c and decreases rapidly with p_T (less than 0.5 % at $p_T > 3$ GeV/c). For PHOS, the π^0 acceptance A is zero for $p_T < 0.4$ GeV/c. The product $\varepsilon \cdot A$ increases with p_T and saturates at about 1.4×10^{-2} for a neutral pion with $p_T > 15$ GeV/c. At high transverse momenta ($p_T > 25$ GeV/c) ε decreases because of merging of clusters of π^0 decay photons due to the decreasing average opening angle of the π^0 decay photons. The correction factor ε does not show a centrality dependence for events in the 20−80 % class, but in the most central bin it increases by ~ 10 % due to an increase in cluster energies caused by cluster overlap.

In the PCM, the photon conversion probability of about 8.6 % is compensated by the large TPC acceptance. Neutral pions were reconstructed in the rapidity interval $|y| < 0.6$ and the decay photons were required to satisfy $|\eta| < 0.65$. The π^0 efficiency increases with p_T below $p_T \approx 4$ GeV/c and remains approximately constant for higher p_T at values between 1.0×10^{-3} in central collisions (0−5 %, energy asymmetry cut $\alpha < 0.65$) and 1.5×10^{-3} in peripheral collisions (60−80 %, $\alpha < 0.8$). For the centrality classes 0−5, 5−10, 10−20, 20−40 %, for which $\alpha < 0.65$ was used, the π^0 efficiency varies between 1.0×10^{-3} and 1.2×10^{-3}. This small centrality dependence is dominated by the centrality dependence of the V0 finding efficiency. Further information on the PHOS and PCM efficiency corrections can be found in [49].

The invariant differential neutral pion yield was calculated as

$$E\frac{d^3N}{d^3p} = \frac{1}{2\pi}\frac{1}{N_{events}}\frac{1}{p_T}\frac{1}{\varepsilon}\frac{1}{A}\frac{1}{Br}\frac{N^{\pi^0}}{\Delta y \Delta p_T}, \quad (2)$$

where N_{events} is the number of events; p_T is the transverse momentum within the bin to which the cross section has been assigned after the correction for the finite bin width Δp_T, Br is the branching ratio of the decay $\pi^0 \to \gamma\gamma$, and N^{π^0} is the number of reconstructed π^0's in a given Δy and Δp_T bin. Finally, the invariant yields were corrected for the finite p_T bin width following the prescription in [59], i.e., by plotting the measured average yield at a p_T position for which the differential invariant yield coincides with the bin average.

Table 1 Summary of the relative systematic uncertainties in percent for selected p_T bins for the PHOS and the PCM analyses

	PHOS					
	pp		Pb–Pb, 60−80 %		Pb–Pb, 0−5 %	
	1.1 GeV/c	7.5 GeV/c	3 GeV/c	10 GeV/c	3 GeV/c	10 GeV/c
Yield extraction	8	2.3	0.8	6.8	3.7	5.7
Photon identification	–	–	1.7	1.7	4.4	4.4
Global E scale	4	6.2	4.1	5.3	6.1	7.8
Non-linearity	9	1.5	1.5	1.5	1.5	1.5
Conversion	3.5	3.5	3.5	3.5	3.5	3.5
Module alignment	4.1	4.1	4.1	4.1	4.1	4.1
Other	2	1.4	2.4	2.4	3.1	3.4
Total	13.9	8.8	7.6	10.7	10.7	12.7
	PCM					
	pp		Pb–Pb, 60−80 %		Pb–Pb, 0−5 %	
	1.1 GeV/c	5.0 GeV/c	1.1 GeV/c	5.0 GeV/c	1.1 GeV/c	5.0 GeV/c
Material budget	9.0	9.0	9.0	9.0	9.0	9.0
Yield extraction	0.6	2.6	3.3	5.9	10.6	5.0
e^+/e^- identification	0.7	1.4	2.9	5.3	9.0	10.5
Photon identification ($\chi^2(\gamma)$)	2.4	0.9	3.7	4.6	4.0	6.7
π^0 reconstruction efficiency	0.5	3.6	3.5	4.1	6.7	8.4
Pile-up correction	1.8	1.8	2.0	2.0	–	–
Total	9.5	10.3	11.4	13.6	18.3	18.2

Secondary π^0's from weak decays or hadronic interactions in the detector material were subtracted using Monte Carlo simulations. The contribution of π^0's from K^0_s as obtained from the used event generators was scaled in order to reproduce the measured K^0_s yields [60]. The correction for secondary π^0's was smaller than 2 % (5 %) for $p_T \gtrsim 2\,\mathrm{GeV/c}$ in the pp as well as in the Pb–Pb analysis for PCM (PHOS).

A summary of the systematic uncertainties for two representative p_T values in pp, peripheral and central Pb–Pb collisions is shown in Table 1. In PHOS, one of the largest sources of the systematic uncertainty both at low and high p_T is the raw yield extraction. It was estimated by varying the fitting range and the assumption about the shape of the background under the peak. In central collisions, major contributions to the systematic uncertainty are due to the efficiency of photon identification and the global energy scale. The former was evaluated by comparing efficiency-corrected π^0 yields, calculated with different identification criteria. The latter was estimated by varying the global energy scale within the tolerance which would still allow to reproduce the peak position in central and peripheral collisions. The uncertainty related to the non-linearity of the PHOS energy response was estimated by introducing different non-linearities into the Monte Carlo simulations under the condition that the simulated p_T dependence of the π^0 peak position and peak width was still consistent with the data. The uncertainty of the PHOS measurement coming from the uncertainty of the fraction of photons lost due to conversion was estimated by comparing measurements without magnetic field to the measurements with magnetic field.

In the PCM measurement, the main sources of systematic uncertainties include the knowledge of the material budget, raw yield extraction, electron identification (PID), the additional photon identification cuts, and π^0 reconstruction efficiency. The uncertainty related to the pile-up correction is only relevant in pp and peripheral Pb–Pb collisions. The contribution from the raw π^0 yield extraction was estimated by changing the normalization range, the integration window, and the combinatorial background evaluation. Uncertainties related to the electron and photon identification cuts, and to the photon reconstruction efficiency were estimated by evaluating the stability of the results for different cuts. The total systematic uncertainties of the PCM and the PHOS results were calculated by adding the individual contributions in quadrature.

The comparisons of the fully corrected π^0 spectra measured by PHOS and PCM in pp and Pb–Pb collisions are presented in Figs. 3 and 4, respectively. For a better comparison the PCM and PHOS data points were divided by a function which was fitted to the combined spectrum. In all

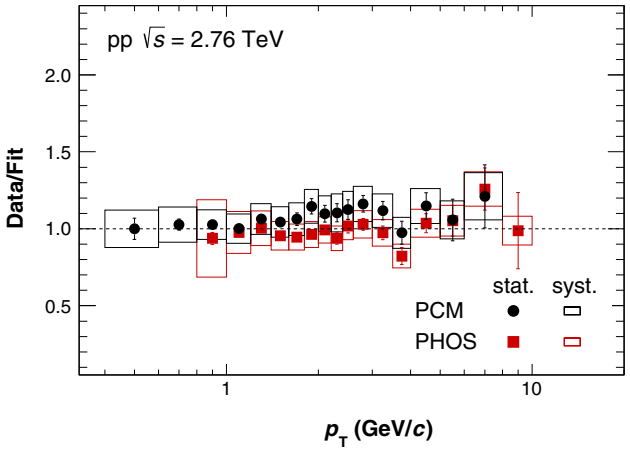

Fig. 3 (Color online) Ratio of the fully corrected π^0 spectra in pp collisions at $\sqrt{s} = 2.76$ TeV measured with PHOS and PCM methods to the fit of the combined spectrum. *Vertical lines* represent statistical uncertainties, the *boxes* systematic uncertainties

cases, agreement between the two measurements is found. The PHOS and PCM spectra were combined by calculating the average yields together with their statistical and systematic uncertainties by using the inverse squares of the total uncertainties of the PHOS and PCM measurements for a given p_T bin as respective weights [40].

4 Results

The invariant neutral pion spectra measured in pp and Pb–Pb collisions are shown in Fig. 5. The p_T range 0.6−12 GeV/c covered by the measurements includes the region $p_T \approx 7$ GeV/c where the charged hadron R_{AA} exhibits the strongest suppression [35–37]. The invariant neutral pion yield in inelastic pp collisions shown in Fig. 5 is related to the invariant cross section as $E\,\mathrm{d}^3\sigma/\mathrm{d}^3p = E\,\mathrm{d}^3N/\mathrm{d}^3p \times \sigma_{\mathrm{inel}}$. Above $p_T \approx 3$ GeV/c the pp spectrum is well described by a power law $E\,\mathrm{d}^3N/\mathrm{d}^3p \propto 1/p_T^n$. A fit to $p_T > 3$ GeV/c yields an exponent $n = 6.0 \pm 0.1$ with $\chi^2/\mathrm{ndf} = 3.8/4$, which is significantly smaller than the value $n = 8.22 \pm 0.09$ observed in pp collisions at $\sqrt{s} = 200$ GeV [31].

Neutral pion production from hard scattering is dominated by the fragmentation of gluon jets in the p_T range of the measurement. The presented π^0 spectrum in pp collisions can therefore help constrain the gluon-to-pion fragmentation function [61]. A next-to-leading-order (NLO) perturbative QCD calculation employing the DSS fragmentation function [62] agrees reasonably well with the measured neutral pion spectrum at $\sqrt{s} = 0.9$ TeV. At $\sqrt{s} = 7$ TeV, however, the predicted invariant cross sections are larger than the measured ones [48]. The comparison to a NLO perturbative QCD calculation using the CTEQ6M5 parton distributions [63] and the DSS fragmentation functions in Fig. 6 shows that the calculation overpredicts the data already at $\sqrt{s} = 2.76$ TeV by a similar factor as in pp collisions at $\sqrt{s} = 7$ TeV. The data are furthermore compared to a PYTHIA 8.176 (tune 4C) [56,64] calculation which reproduces the shape of the spectrum with an overall offset of about 20 %. It will be interesting to see whether calculations in the framework of the color glass condensate [65], which describe the neutral pion spectrum in pp collisions at $\sqrt{s} =$

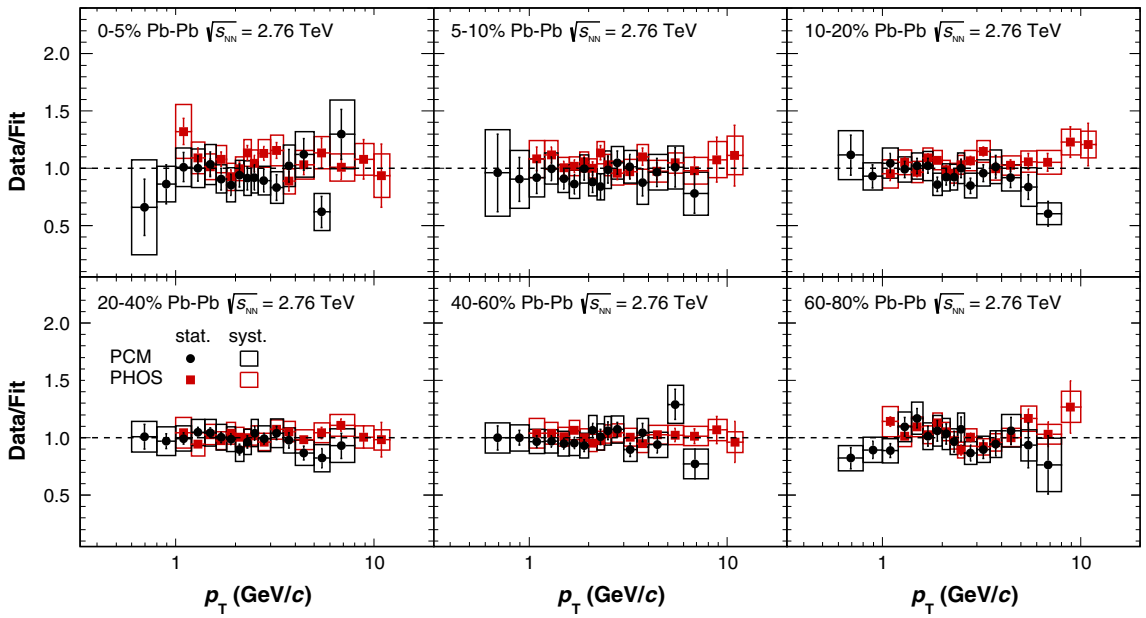

Fig. 4 (Color online) Ratio of the fully corrected π^0 spectra in Pb–Pb collisions at $\sqrt{s_{NN}} = 2.76$ TeV in six centrality bins measured with PHOS and PCM to the fits to the combined result in each bin. *Vertical lines* represent statistical uncertainties, the *boxes* the systematic uncertainties

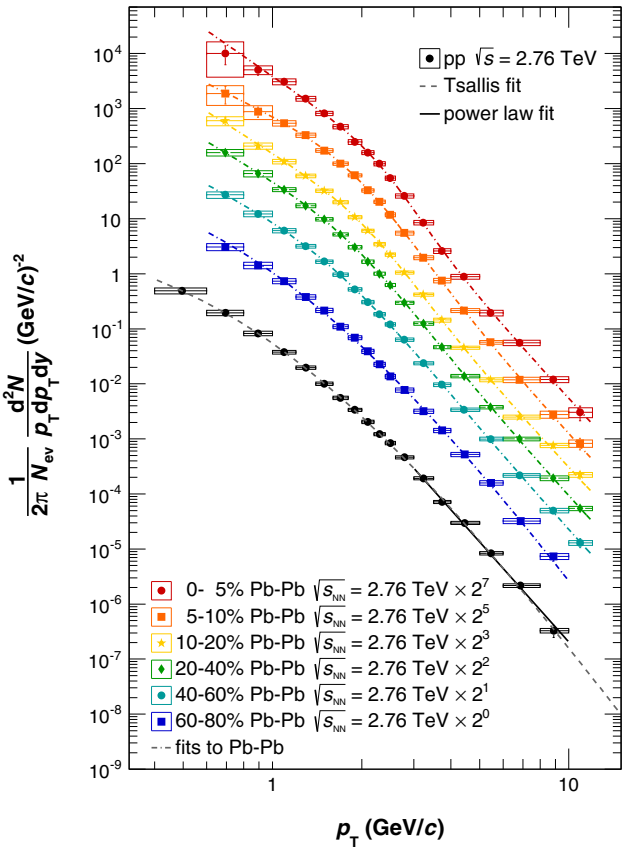

Fig. 5 (Color online) Invariant differential yields of neutral pions produced in Pb–Pb and inelastic pp collisions at $\sqrt{s_{NN}} = 2.76$ TeV. The spectra are the weighted average of the PHOS and the PCM results. The *vertical lines* show the statistical uncertainties, systematic uncertainties are shown as *boxes*. *Horizontal lines* indicate the bin width. The horizontal position of the data points within a bin was determined by the procedure described in [59]. For the pp spectrum a fit with a power law function $1/p_T^n$ for $p_T > 3$ GeV/c and a Tsallis function (also used in [48]) are shown. The extrapolation of the pp spectrum provided by the Tsallis fit is used in the R_{AA} calculation for $p_T \gtrsim 8$ GeV/c

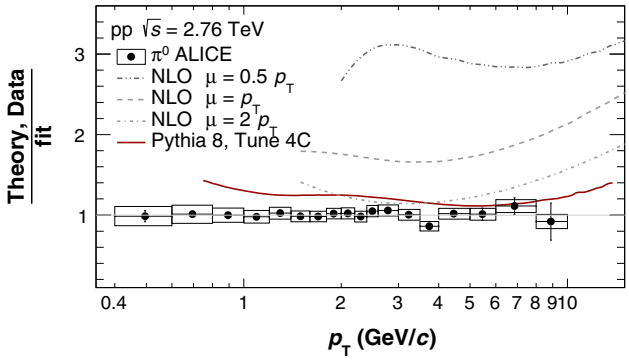

Fig. 6 (Color online) Ratio of data or theory calculations to a fit of the neutral pion spectrum in pp collisions at $\sqrt{s_{NN}} = 2.76$ TeV. The renormalization, factorization, and fragmentation scale of the next-to-leading order QCD calculation were varied simultaneously ($\mu = 0.5 p_T$, p_T, $2p_T$). The calculation employed the CTEQ6M5 [63] parton distribution functions and the DSS fragmentation function [62]. The *solid red line* is a comparison to the PYTHIA 8.176 (tune 4C) event generator [56,64]

Table 2 Values for the overlap function $\langle T_{AA} \rangle$ for the centrality bins used in this analysis

Centrality class (%)	$\langle T_{AA} \rangle$ (1/mb)	Rel. syst. uncert. (%)
0–5	26.32	3.2
5–10	20.56	3.3
10–20	14.39	3.1
20–40	6.85	3.3
40–60	1.996	4.9
60–80	0.4174	6.2

7 TeV, will also provide a good description of the data at $\sqrt{s} = 2.76$ TeV.

The nuclear modification factor, R_{AA}, was calculated according to Eq. 1. For $p_T > 8$ GeV/c the extrapolation of the pp spectrum provided by the power law fit shown in Fig. 5 was used as a reference. The systematic uncertainty of the extrapolation was estimated based on the variation of the fit range ($p_T > 2, 3, 4$ GeV/c) and the systematic uncertainty in the bin from $p_T = 6$–8 GeV/c. The average values of the nuclear overlap function T_{AA} for each centrality class were taken from [46] and are given in Table 2. They were determined with a Glauber Monte Carlo calculation [66,67] by defining percentiles with respect to the simulated impact parameter b and therefore represent purely geometric quantities.

The combined R_{AA} was calculated as a weighted average of the individual R_{AA} measured with PHOS and PCM. This has the advantage of reduced systematic uncertainties of the combined result. In particular, the dominant uncertainty in the PCM, related to the material budget, cancels this way. The results for the combined R_{AA} are shown in Fig. 7. In all centrality classes the measured R_{AA} exhibits a maximum around $p_T \approx 1$–2 GeV/c, a decrease in the range $2 \lesssim p_T \lesssim 3$–$6$ GeV/c, and an approximately constant value in the measured p_T range for higher p_T. For $p_T \gtrsim 6$ GeV/c, where particle production is expected to be dominated by fragmentation of hard-scattered partons, R_{AA} decreases with centrality from about $0.5-0.7$ in the 60–80 % class to about 0.1 in the 0-5 % class. The R_{AA} measurements for neutral pions and charged pions [68] agree with each other over the entire p_T range for all centrality classes. Agreement between the neutral pion and charged particle R_{AA} [37] is observed for $p_T \gtrsim 6$ GeV/c.

It is instructive to study the $\sqrt{s_{NN}}$ dependence of the neutral pion R_{AA}. Figure 8 shows that for central collisions the R_{AA} at the LHC for $p_T \gtrsim 2$ GeV/c lies below the data points at lower $\sqrt{s_{NN}}$. This indicates that the decrease of R_{AA} resulting from the higher initial energy densities created at larger

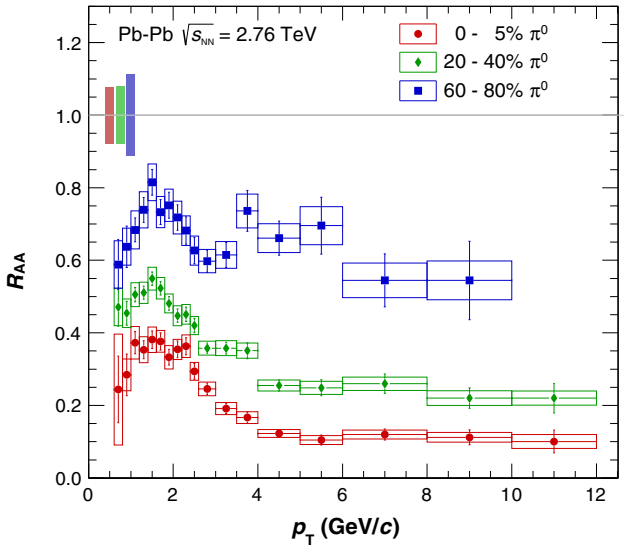

Fig. 7 (Color online) Neutral pion nuclear modification factor R_{AA} for three different centralities (0−5, 20−40, 60−80 %) in Pb–Pb collisions at $\sqrt{s_{NN}} = 2.76$ TeV. *Vertical error bars* reflect statistical uncertainties, *boxes* systematic uncertainties. *Horizontal bars* reflect the bin width. The *boxes* around unity reflect the uncertainty of the average nuclear overlap function (T_{AA}) and the normalization uncertainty of the pp spectrum added in quadrature

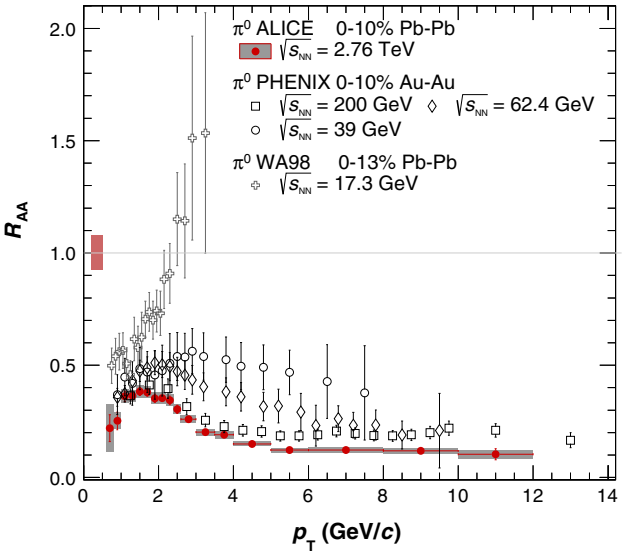

Fig. 8 (Color online) Neutral pion nuclear modification factor, R_{AA}, in Pb–Pb collisions at $\sqrt{s_{NN}} = 2.76$ TeV for the 0−10 % class in comparison to results at lower energies. The *box* around unity reflects the uncertainty of the average nuclear overlap function (T_{AA}) and the normalization uncertainty of the pp spectrum added in quadrature. *Horizontal bars* reflect the bin width. The center-of-mass energy dependence of the neutral pion R_{AA} is shown with results from Au–Au collisions at $\sqrt{s_{NN}} = 39$, 62.4 [34], and 200 GeV [31] as well as the result from the CERN SPS [69] (using scaled p-C data as reference) along with the results for Pb–Pb at $\sqrt{s_{NN}} = 2.76$ TeV. The scale uncertainties of the measurements at lower energies of the order of 10−15 % are not shown

$\sqrt{s_{NN}}$ dominates over the increase of R_{AA} expected from the harder initial parton p_T spectra. To illustrated this point, one can consider a somewhat oversimplified model with a p_T independent fractional energy loss ε in conjunction with p_T spectra described by a power law [70]. In this model $\varepsilon = 0.2$ corresponds to $R_{AA}^{RHIC} \approx 0.25$ at $\sqrt{s_{NN}} = 0.2$ TeV. The same fractional energy loss in conjunction with the flatter spectra at $\sqrt{s_{NN}} = 2.76$ TeV, however, yield $R_{AA}^{LHC} \approx 0.4$. The shape of $R_{AA}(p_T)$ in central collisions at $\sqrt{s_{NN}} = 200$ GeV and $\sqrt{s_{NN}} = 2.76$ TeV appears to be similar. Considering the data for all shown energies one observes that the value of p_T with the maximum R_{AA} value appears to shift towards lower p_T with increasing $\sqrt{s_{NN}}$. The centrality dependence of R_{AA} at $p_T = 7$ GeV/c is shown in Fig. 9 for nuclear collisions at $\sqrt{s_{NN}} = 39$, 62.4, 200 [22,34], and 2,760 GeV. At this transverse momentum soft particle production from the bulk should be negligible and parton energy loss is expected to be the dominant effect. It can be seen that the suppression in Pb–Pb collisions at the LHC is stronger than in Au–Au collisions at $\sqrt{s_{NN}} = 200$ GeV for all centralities. In particular, the most peripheral class of the LHC data already shows a sizable suppression whereas at the lower energies the suppression appears to develop less abruptly as a function of the number of participating nucleons (N_{part}).

In Fig. 10 the measured R_{AA} is compared with a GLV model calculation [38,39] and with theoretical predictions from the WHDG model [71]. These models describe the interaction of a hard-scattered parton with the medium of high color charge density within perturbative QCD [11].

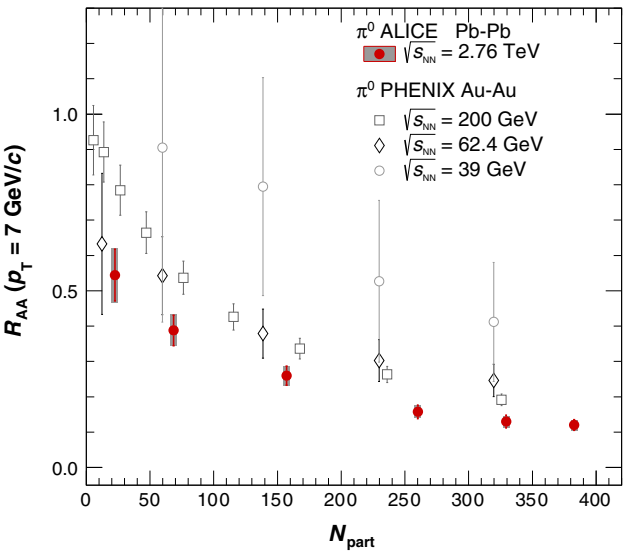

Fig. 9 (Color online) Centrality dependence of the π^0 nuclear modification factor R_{AA} at $p_T = 7$ GeV/c in Au–Au and Pb–Pb collisions at $\sqrt{s_{NN}} = 39$, 62.4, 200 [22,34], and 2,760 GeV

Both calculations assume that the hadronization of the hard-scattered parton occurs in the vacuum and is not affected by the medium. They model the energy loss of the parton but not the corresponding response of the medium. Their appli-

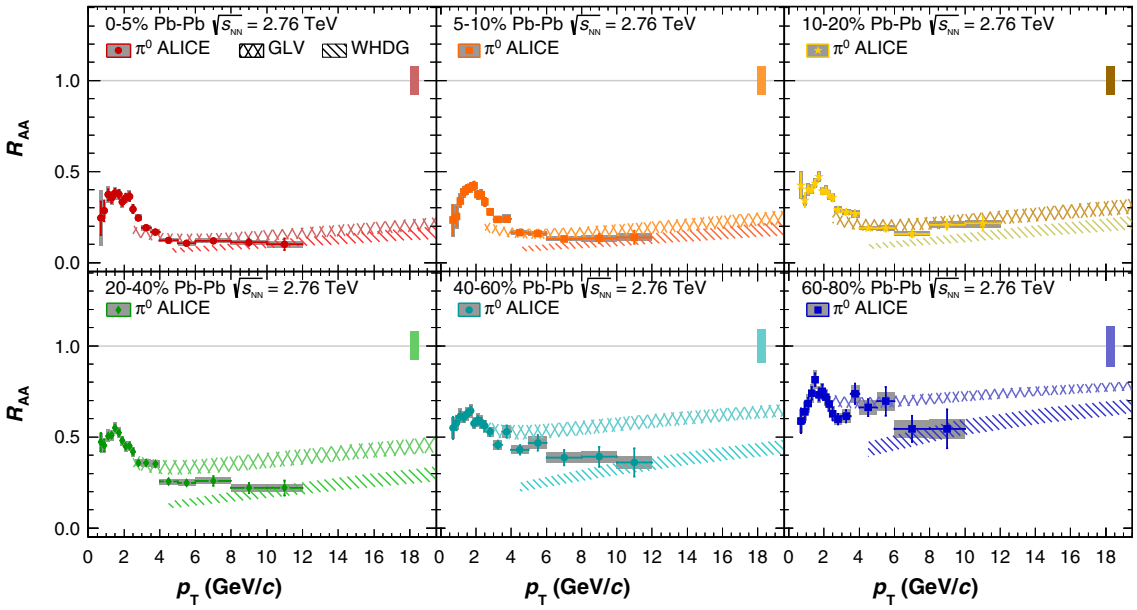

Fig. 10 (Color online) Comparison of the measured nuclear modification factor R_{AA} with a GLV calculation [38,39] and with a WHDG [71] parton energy loss calculations. *Vertical lines* show the statistical uncertainties, systematic uncertainties are shown as *boxes*. *Horizontal lines* indicate the bin width. The *boxes* around unity reflect the scale uncertainties of data related to T_{AA} and the normalization of the pp spectrum

cability is limited to transverse momenta above 2−4 GeV/c as soft particle production from the bulk is not taken into account. The Pb–Pb π^0 spectra are therefore also compared to two models which aim at a description of the full p_{T} range: an EPOS calculation [72] and a calculation by Nemchik et al. based on the combination of a hydrodynamic description at low p_{T} and the absorption of color dipoles at higher p_{T} [73,74]. These comparisons are presented in Fig. 11.

The GLV calculation takes final-state radiative energy loss into account. It includes the broadening of the transverse momenta of the incoming partons in cold nuclear matter ("nuclear broadening" or "Cronin effect"). The main parameter of this model, the initial gluon density, was tuned to describe the neutral pion suppression observed in Au–Au collisions at RHIC. For the calculation of the parton energy loss in Pb–Pb collisions at the LHC the initial gluon density was constrained by the measured charged-particle multiplicities. The model can approximately reproduce the centrality and p_{T} dependence of the π^0 R_{AA}.

The WHDG model takes into account collisional and radiative parton energy loss and geometrical path length fluctuations. The color charge density of the medium is assumed to be proportional to the number of participating nucleons from a Glauber model, and hard parton-parton scatterings are proportional to the number of binary nucleon-nucleon collisions. Parameters of the model were constrained by the neutral pion R_{AA} measured at RHIC. Like in the case of the GLV calculation, the neutral pion R_{AA} at the LHC is then predicted by translating the measured charged-particle multiplicity $\mathrm{d}N_{ch}/\mathrm{d}\eta$ in Pb–Pb collisions into an initial gluon density which is the free parameter of the model. For central collisions this yielded an increase in the gluon density from $\mathrm{d}N_g/\mathrm{d}y \approx 1400$ at RHIC to $\mathrm{d}N_g/\mathrm{d}y \approx 3{,}000$ at the LHC. The WHDG model reproduces the π^0 R_{AA} in central collisions reasonably well, but predicts too strong suppression for more peripheral classes.

The two model predictions for the full p_{T} range are compared to the measured spectra in Fig. 11. EPOS is based on the hadronization of flux tubes produced early in the collision. Hard scattering in this model produces strings with transversely moving parts. String segments with low energies are assumed to be part of the bulk whose space-time evolution is modeled within hydrodynamics. String segments with sufficiently large energy fragment in the vacuum. A third class of string segments with intermediate energies is considered to have enough energy to leave the medium accompanied by quark pick-up from the bulk during the fragmentation process. In EPOS particle production is determined by hydrodynamic flow at low p_{T} ($\lesssim$4 GeV/c), followed at higher p_{T} by energy loss of high-p_{T} string segments. In central collisions the EPOS calculation describes the measured π^0 spectrum rather well. Towards more peripheral collisions a discrepancy develops for $1 \lesssim p_{\mathrm{T}} \lesssim 5$ GeV/c which may possibly be attributed to underestimating the contribution of hydrodynamic flow in peripheral collisions.

The calculation by Nemchik et al. also combines a model for hadron suppression at high p_{T} with a hydrodynamic description of bulk particle production at low p_{T}. Hadron

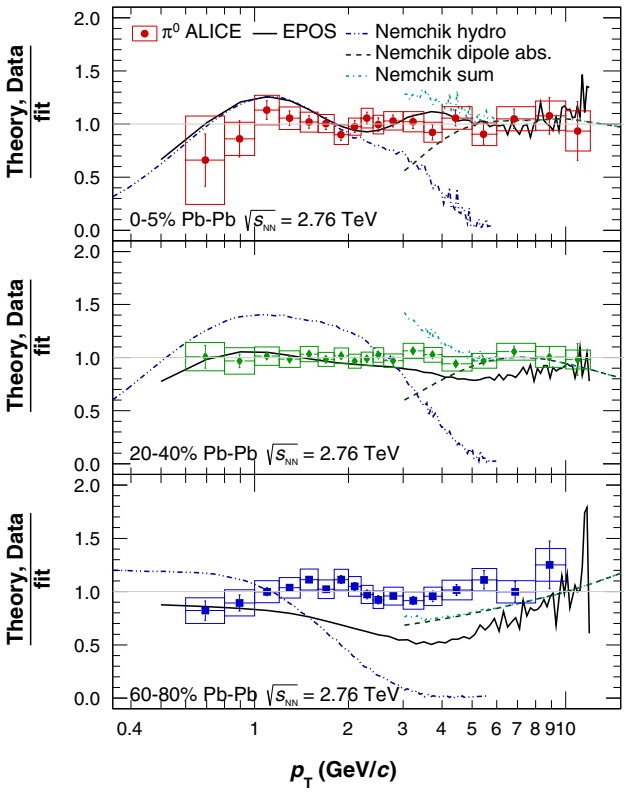

Fig. 11 (Color online) Comparison of the measured π^0 spectra for three centrality classes (0−5, 20−40, 60−80 %) with two calculations which make predictions for the full p_T range of the measurement. The calculated spectra and the data points were divided by a fit of the measured π^0 spectra. For the data points the *error bars* represent the statistical uncertainties and the *boxes* the systematic uncertainties. Calculations with the EPOS event generator [72] are shown by the *solid line*. The fluctuations of the EPOS lines at high p_T are due to limited statistics in the number of generated events. The calculations by Nemchik et al. [73,74] combine a hydrodynamical model at low p_T with a color dipole absorption model for $p_T \gtrsim 3$ GeV/c. The two components and the sum (for $p_T \gtrsim 3$ GeV/c) are shown separately

suppression in this model results from the absorption of prehadrons, i.e., of color dipoles which are already formed in the medium by hard-scattered partons during the production of hadrons with large $z = p_{\mathrm{hadron}}/p_{\mathrm{parton}}$. As the model, at high p_T, predicts only R_{AA}, the calculated R_{AA} values were scaled by $\langle T_{AA}\rangle \times E\,\mathrm{d}^3\sigma^{\pi^0}_{\mathrm{meas}}/\mathrm{d}^3p$ and then added to the calculated π^0 invariant yields from the hydrodynamic model in order to compare to the measured π^0 spectra. The hydrodynamic calculation dominates the total π^0 yield up to $p_T = 2$ GeV/c and remains a significant contribution up to 5 GeV/c. From about 3 GeV/c the contribution from hard scattering becomes larger than the one from the hydrodynamic calculation. The spectrum in central Pb–Pb collisions (0−5 %) is approximately described except for the transition region between the hydrodynamic and the hard contribution. In the 20−40 % class the hydrodynamic calculation overpredicts the data up to $p_T = 2$ GeV/c.

5 Conclusions

Measurements of neutral pion production at midrapidity in pp and Pb–Pb collisions at $\sqrt{s_{NN}} = 2.76$ TeV were presented. The measurements were performed with two independent techniques, by measuring the photons with the electromagnetic calorimeter PHOS, and by measuring converted photons with the ALICE tracking system. The two independent measurements were found to give consistent results, and were combined for the final results.

The neutral pion spectrum in pp collisions was compared to a NLO perturbative QCD calculation using the DSS fragmentation functions. This calculation, which describes the pion spectrum in pp collisions at $\sqrt{s} = 0.9$ TeV rather well, tends to overpredict the π^0 cross section already at $\sqrt{s} = 2.76$ TeV. Along with a similar observation in pp collision at $\sqrt{s} = 7$ TeV this indicates the likely need for improvements in the gluon-to-pion fragmentation function. A similar observation was made for transverse momentum spectra of charged particles in proton-proton and proton-antiproton collisons at $1.96 \lesssim \sqrt{s} \lesssim 7$ TeV [61,75].

The neutral pion nuclear suppression factor R_{AA} was calculated from the measured neutral pion spectra, and was compared to measurements at lower energies and to theoretical predictions. The π^0 suppression in the most central class (0−5 %) reaches values of up to 8−10 for $5 \lesssim p_T \lesssim 7$ GeV/c. The suppression in Pb–Pb collisions at $\sqrt{s_{NN}} = 2.76$ TeV is stronger than in Au–Au collisions at $\sqrt{s_{NN}} = 200$ GeV (and lower energies) at RHIC for all centralities.

The general features of the centrality and p_T dependence of the R_{AA} for $p_T \gtrsim 2$ GeV/c are approximately reproduced by GLV and WHDG parton energy loss calculations, although the WHDG calculation performs less well in peripheral collisions. For both calculations the main free parameter, the initial gluon density, was chosen to describe the neutral pion suppression at RHIC and then scaled to LHC energies based on the measured charged-particle multiplicities. The measured π^0 spectra were also compared to calculations with the EPOS event generator and a calculation by Nemchik et al. By combining soft particle production from a hydrodynamically evolving medium with a model for hadron suppression these models are capable of making predictions for the entire p_T range. An important task on the theoretical side will be to establish whether the observed deviations from the data simply indicate a suboptimal adjustment of parameters or hint at important physical phenomena missing in the models. Future analyses based on runs with higher integrated luminosities, e.g. the 2011 LHC Pb–Pb run, will also include the ALICE lead-scintillator electromagnetic calorimeter (EMCal) and will allow us to extend the neutral pion measurement to higher transverse momenta. The role of initial-state effects on the particle production in Pb–Pb

collisions will be investigated by measurements of particle production in p-Pb collisions.

Acknowledgments We would like to thank Jan Nemchik, William A. Horowitz, Ivan Vitev, and Klaus Werner for providing the model calculations shown in this paper. This work was supported by the grants RFBR 10-02-91052 and RFBR 12-02-91527. The ALICE Collaboration would like to thank all its engineers and technicians for their invaluable contributions to the construction of the experiment and the CERN accelerator teams for the outstanding performance of the LHC complex. The ALICE Collaboration gratefully acknowledges the resources and support provided by all Grid centres and the Worldwide LHC Computing Grid (WLCG) collaboration. The ALICE Collaboration acknowledges the following funding agencies for their support in building and running the ALICE detector: State Committee of Science, World Federation of Scientists (WFS) and Swiss Fonds Kidagan, Armenia, Conselho Nacional de Desenvolvimento Científico e Tecnológico (CNPq), Financiadora de Estudos e Projetos (FINEP), Fundação de Amparo à Pesquisa do Estado de São Paulo (FAPESP); National Natural Science Foundation of China (NSFC), the Chinese Ministry of Education (CMOE) and the Ministry of Science and Technology of China (MSTC); Ministry of Education and Youth of the Czech Republic; Danish Natural Science Research Council, the Carlsberg Foundation and the Danish National Research Foundation; The European Research Council under the European Community's Seventh Framework Programme; Helsinki Institute of Physics and the Academy of Finland; French CNRS-IN2P3, the 'Region Pays de Loire', 'Region Alsace', 'Region Auvergne' and CEA, France; German BMBF and the Helmholtz Association; General Secretariat for Research and Technology, Ministry of Development, Greece; Hungarian OTKA and National Office for Research and Technology (NKTH); Department of Atomic Energy and Department of Science and Technology of the Government of India; Istituto Nazionale di Fisica Nucleare (INFN) and Centro Fermi - Museo Storico della Fisica e Centro Studi e Ricerche "Enrico Fermi", Italy; MEXT Grant-in-Aid for Specially Promoted Research, Japan;
Joint Institute for Nuclear Research, Dubna; National Research Foundation of Korea (NRF); CONACYT, DGAPA, México, ALFA-EC and the EPLANET Program (European Particle Physics Latin American Network) Stichting voor Fundamenteel Onderzoek der Materie (FOM) and the Nederlandse Organisatie voor Wetenschappelijk Onderzoek (NWO), The Netherlands; Research Council of Norway (NFR); Polish Ministry of Science and Higher Education; National Science Centre, Poland; Ministry of National Education/Institute for Atomic Physics and CNCS-UEFISCDI - Romania; Ministry of Education and Science of Russian Federation, Russian Academy of Sciences, Russian Federal Agency of Atomic Energy, Russian Federal Agency for Science and Innovations and The Russian Foundation for Basic Research; Ministry of Education of Slovakia; Department of Science and Technology, South Africa; CIEMAT, EELA, Ministerio de Economía y Competitividad (MINECO) of Spain, Xunta de Galicia (Consellería de Educación), CEADEN, Cubaenergía, Cuba, and IAEA (International Atomic Energy Agency); Swedish Research Council (VR) and Knut & Alice Wallenberg Foundation (KAW); Ukraine Ministry of Education and Science; United Kingdom Science and Technology Facilities Council (STFC); The United States Department of Energy, the United States National Science Foundation, the State of Texas, and the State of Ohio.

6 Appendix

For the calculation of the R_{AA} above $p_{\mathrm{T}} > 8\,\mathrm{GeV/c}$ an extrapolation of the measured transverse momentum spectrum in pp collisions at $\sqrt{s} = 2.76\,\mathrm{TeV}$ based on the Tsallis functional form

$$\frac{1}{2\pi p_{\mathrm{T}}}\frac{\mathrm{d}^2N}{\mathrm{d}p_{\mathrm{T}}\mathrm{d}y} = \frac{A}{2\pi}\frac{(n-1)(n-2)}{nC\,[nC+m(n-2)]}\frac{1}{c^2} \cdot \left(1+\frac{\sqrt{p_{\mathrm{T}}^2+m^2}-m}{nC}\right)^{-n} \tag{3}$$

was used (where m is the mass of the neutral pion and c the speed of light). The parameters are given in Table 3.

In order to compare the individual PCM and PHOS measurements to the combined results in Pb–Pb collisions the parameterization

$$\frac{1}{2\pi p_{\mathrm{T}}}\frac{\mathrm{d}^2N}{\mathrm{d}p_{\mathrm{T}}\mathrm{d}y} = a \cdot p_{\mathrm{T}}^{-(b+c/(p_{\mathrm{T}}^d+e))} \tag{4}$$

with p_{T} in GeV/c was used to fit the combined spectrum for each centrality class. The corresponding parameters are given

Table 3 Parameters of the fits of the Tsallis parameterization (Eq. 3) to the combined invariant production yields for π^0 mesons in inelastic collisions at $\sqrt{s} = 2.76\,\mathrm{TeV}$

System	A	C (MeV/c^2)	n
pp	1.7 ± 0.7	135 ± 29	7.1 ± 0.7
60−80 % Pb–Pb	31.7	142	7.4

The uncertainties (statistical and systematic added in quadrature) were used to evaluate the uncertainty of the extrapolation used in the calculation of R_{AA} for $p_{\mathrm{T}} > 8\,\mathrm{GeV/c}$. The uncertainty on the parameter A due to the spectra normalization of 3.9 % at $\sqrt{s} = 2.76\,\mathrm{TeV}$ is not included. For the measurment in 60−80 % Pb–Pb collisions the fit parameters are given without uncertainties as the parameterization is only used to facilitate the comparison with model calculations

Table 4 Parameters of the fits to the combined invariant yields of π^0 mesons in Pb–Pb collisions in different centrality classes with the functional form given in Eq. 4

Centrality (%)	a (c^2/GeV^2)	b	c	d	e
0−5	28.96	5.85	−199.17	4.64	95.30
5−10	21.97	5.79	−33.54	2.96	10.84
0−10	25.53	5.84	−49.95	3.35	18.49
10−20	18.91	5.71	−44.76	3.37	19.66
20−40	11.54	5.74	−18.43	2.62	7.37
40−60	4.18	5.67	−9.43	2.00	3.39

The spectra were fitted taking into account the combined statistical and systematic errors

in Table 4. For the most peripheral centrality class the Tsallis parameterization Eq. 3 was used for which the parameters are given in Table 3. These parameterizations describe the data well in the measured momentum range.

References

1. S. Borsanyi, G. Endrodi, Z. Fodor, A. Jakovac, S.D. Katz et al., JHEP **1011**, 077 (2010). doi:10.1007/JHEP11(2010)077
2. A. Bazavov, T. Bhattacharya, M. Cheng, C. DeTar, H. Ding et al., Phys. Rev. D **85**, 054503 (2012). doi:10.1103/PhysRevD.85.054503
3. S. Chatrchyan et al., Phys. Rev. Lett. **109**, 152303 (2012). doi:10.1103/PhysRevLett.109.152303
4. A. Toia for the ALICE collaboration, J. Phys. G **38**, 124007 (2011). doi:10.1088/0954-3899/38/12/124007
5. U. Heinz, R. Snellings, Ann. Rev. Nucl. Part. Sci. **63**, 123 (2013). doi:10.1146/annurev-nucl-102212-170540
6. J. Bjorken, FERMILAB-PUB-82-059-THY (1982)
7. X.N. Wang, M. Gyulassy, Phys. Rev. Lett. **68**, 1480 (1992). doi:10.1103/PhysRevLett.68.1480
8. U.A. Wiedemann, in *SpringerMaterials—The Landolt–Börnstein Database*. ed. by R. Stock. Relativistic Heavy Ion Physics, vol. 23 (Springer, Berlin, 2009). doi:10.1007/978-3-642-01539-7_17
9. D. d'Enterria, in *SpringerMaterials—The Landolt–Börnstein Database*, ed. by R. Stock Relativistic Heavy Ion Physics, vol. 23 (Springer, Berlin, 2009). doi:10.1007/978-3-642-01539-7_16
10. A. Majumder, M. Van Leeuwen, Prog. Part. Nucl. Phys. A **66**, 41 (2011). doi:10.1016/j.ppnp.2010.09.001
11. N. Armesto, B. Cole, C. Gale, W.A. Horowitz, P. Jacobs et al., Phys. Rev. C **86**, 064904 (2012). doi:10.1103/PhysRevC.86.064904
12. K.M. Burke, A. Buzzatti, N. Chang, C. Gale, M. Gyulassy, et al. Extracting jet transport coefficient from jet quenching at RHIC and LHC. Preprint NT-LBNL-13-011, arXiv:1312.5003 (2013)
13. B. Abelev et al., Phys. Rev. Lett. **110**, 082302 (2013). doi:10.1103/PhysRevLett.110.082302
14. W. Horowitz, M. Gyulassy, Nucl. Phys. A **872**, 265 (2011). doi:10.1016/j.nuclphysa.2011.09.018
15. R. Sassot, P. Zurita, M. Stratmann, Phys. Rev. D **82**, 074011 (2010). doi:10.1103/PhysRevD.82.074011
16. R. Sassot, M. Stratmann, P. Zurita, Phys. Rev. D **81**, 054001 (2010). doi:10.1103/PhysRevD.81.054001
17. S. Sapeta, U.A. Wiedemann, Eur. Phys. J. C **55**, 293 (2008). doi:10.1140/epjc/s10052-008-0592-8
18. R. Bellwied, C. Markert, Phys. Lett. B **691**, 208 (2010). doi:10.1016/j.physletb.2010.06.028
19. K. Adcox et al., Phys. Rev. Lett. **88**, 022301 (2002). doi:10.1103/PhysRevLett.88.022301
20. C. Adler et al., Phys. Rev. Lett. **89**, 202301 (2002). doi:10.1103/PhysRevLett.89.202301
21. G. Agakishiev et al., Phys. Rev. Lett. **108**, 072302 (2012). doi:10.1103/PhysRevLett.108.072302
22. A. Adare et al., Phys. Rev. C **87**, 034911 (2013). doi:10.1103/PhysRevC.87.034911
23. A. Adare et al., Phys. Rev. C **88**, 024906 (2013). doi:10.1103/PhysRevC.88.024906
24. C. Adler et al., Phys. Rev. Lett. **90**, 082302 (2003). doi:10.1103/PhysRevLett.90.082302
25. J. Adams et al., Phys. Rev. Lett. **97**, 162301 (2006). doi:10.1103/PhysRevLett.97.162301
26. I. Arsene et al., Nucl. Phys. A **757**, 1 (2005). doi:10.1016/j.nuclphysa.2005.02.130
27. K. Adcox et al., Nucl. Phys. A **757**, 184 (2005). doi:10.1016/j.nuclphysa.2005.03.086
28. B. Back, M. Baker, M. Ballintijn, D. Barton, B. Becker et al., Nucl. Phys. A **757**, 28 (2005). doi:10.1016/j.nuclphysa.2005.03.084
29. J. Adams et al., Nucl. Phys. A **757**, 102 (2005). doi:10.1016/j.nuclphysa.2005.03.085
30. S.S. Adler et al., Phys. Rev. Lett. **91**, 072301 (2003). doi:10.1103/PhysRevLett.91.072301
31. A. Adare et al., Phys. Rev. Lett. **101**, 232301 (2008). doi:10.1103/PhysRevLett.101.232301
32. S.A. Bass, C. Gale, A. Majumder, C. Nonaka, G.Y. Qin et al., Phys. Rev. C **79**, 024901 (2009). doi:10.1103/PhysRevC.79.024901
33. A. Adare et al., Phys. Rev. Lett. **101**, 162301 (2008). doi:10.1103/PhysRevLett.101.162301
34. A. Adare et al., Phys. Rev. Lett. **109**, 152301 (2012). doi:10.1103/PhysRevLett.109.152301
35. K. Aamodt et al., Phys. Lett. B **696**, 30 (2011). doi:10.1016/j.physletb.2010.12.020
36. S. Chatrchyan et al., Eur. Phys. J. C **72**, 1945 (2012). doi:10.1140/epjc/s10052-012-1945-x
37. B. Abelev et al., Phys. Lett. B **720**, 52 (2013). doi:10.1016/j.physletb.2013.01.051
38. R. Sharma, I. Vitev, B.W. Zhang, Phys. Rev. C **80**, 054902 (2009). doi:10.1103/PhysRevC.80.054902
39. R. Neufeld, I. Vitev, B.W. Zhang, Phys. Lett. B **704**, 590 (2011). doi:10.1016/j.physletb.2011.09.045
40. J. Beringer et al., Phys. Rev. D **86**, 010001 (2012). doi:10.1103/PhysRevD.86.010001
41. G. Dellacasa, et al., CERN-LHCC-99-04 (1999)
42. K. Aamodt et al., JINST **5**, P03003 (2010). doi:10.1088/1748-0221/5/03/P03003
43. J. Alme, Y. Andres, H. Appelshauser, S. Bablok, N. Bialas et al., Nucl. Instrum. Meth. A **622**, 316 (2010). doi:10.1016/j.nima.2010.04.042
44. K. Aamodt et al., JINST **3**, S08002 (2008). doi:10.1088/1748-0221/3/08/S08002
45. P. Cortese, et al., CERN-LHCC-2004-025 (2004)
46. B. Abelev et al., Phys. Rev. C **88**, 044909 (2013). doi:10.1103/PhysRevC.88.044909
47. B. Abelev et al., Eur. Phys. J. C **73**, 2456 (2013). doi:10.1140/epjc/s10052-013-2456-0
48. B. Abelev et al., Phys. Lett. B **717**, 162 (2012). doi:10.1016/j.physletb.2012.09.015
49. B. Abelev, et al. Performance of the ALICE experiment at the CERN LHC. Preprint CERN-PH-EP-2014-031. arXiv:1402.4476 (2014)
50. R. Brun, F. Bruyant, M. Maire, A. McPherson, P. Zanarini, GEANT3. Tech. rep., CERN. CERN-DD-EE-84-1 (1987)
51. E. Alessandro, G, et al., J. Phys. G **32**, 1295. doi:10.1088/0954-3899/32/10/001
52. S. Gorbunov, I. Kisel, Reconstruction of decayed particles based on the Kalman filter. Tech. rep., CBM experiment. CBM-SOFT-note-2007-003 (2007)
53. J. Podolanski, R. Armenteros, Philos. Mag. **45**(360), 13 (1954)
54. M.J. Oreglia, A study of the reactions $\psi' \to \gamma\gamma\psi$. Ph.D. thesis, SLAC, Stanford University, Stanford, California 94305 (1980). http://www.slac.stanford.edu/pubs/slacreports/slac-r-236.html
55. K. Koch, Nucl. Phys. A **855**, 281 (2011). doi:10.1016/j.nuclphysa.2011.02.059
56. T. Sjostrand, S. Mrenna, P.Z. Skands, Comput. Phys. Commun. **178**, 852 (2008). doi:10.1016/j.cpc.2008.01.036
57. R. Engel, J. Ranft, S. Roesler, Phys. Rev. D **52**, 1459 (1995). doi:10.1103/PhysRevD.52.1459
58. M. Gyulassy, X.N. Wang, Comput. Phys. Commun. **83**, 307 (1994). doi:10.1016/0010-4655(94)90057-4

59. G. Lafferty, T. Wyatt, Nucl. Instrum. Meth. A **355**, 541 (1995). doi:10.1016/0168-9002(94)01112-5
60. B. Abelev et al., Phys. Rev. Lett. **111**, 222301 (2013). doi:10.1103/PhysRevLett.111.222301
61. D. d'Enterria, K.J. Eskola, I. Helenius, H. Paukkunen, Nucl. Phys. B **883**, 615 (2014). doi:10.1016/j.nuclphysb.2014.04.006
62. D. de Florian, R. Sassot, M. Stratmann, Phys. Rev. D **75**, 114010 (2007). doi:10.1103/PhysRevD.75.114010
63. J. Pumplin, D. Stump, J. Huston, H. Lai, P.M. Nadolsky et al., JHEP **0207**, 012 (2002). doi:10.1088/1126-6708/2002/07/012
64. R. Corke, T. Sjostrand, JHEP **1103**, 032 (2011). doi:10.1007/JHEP03(2011)032
65. T. Lappi, H. Mantysaari. Phys. Rev. D **88**, 114020 (2013). doi:10.1103/PhysRevD.88.114020
66. M.L. Miller, K. Reygers, S.J. Sanders, P. Steinberg, Ann. Rev. Nucl. Part. Sci. **57**, 205 (2007). doi:10.1146/annurev.nucl.57.090506.123020
67. B. Alver, M. Baker, C. Loizides, P. Steinberg, nucl-ex/0805.4411 (2008)
68. B. Abelev, et al., arXiv:1401.1250 (2014)
69. M. Aggarwal et al., Phys. Rev. Lett. **100**, 242301 (2008). doi:10.1103/PhysRevLett.100.242301
70. S. Adler et al., Phys. Rev. C **76**, 034904 (2007). doi:10.1103/PhysRevC.76.034904
71. W.A. Horowitz, Int. J. Mod. Phys. E **16**, 2193 (2007). doi:10.1142/S0218301307007672
72. K. Werner, I. Karpenko, M. Bleicher, T. Pierog, S. Porteboeuf-Houssais, Phys. Rev. C **85**, 064907 (2012). doi:10.1103/PhysRevC.85.064907
73. B. Kopeliovich, J. Nemchik, I. Potashnikova, I. Schmidt, Phys. Rev. C **86**, 054904 (2012). doi:10.1103/PhysRevC.86.054904
74. J. Nemchik, I.A. Karpenko, B. Kopeliovich, I. Potashnikova, Y.M. Sinyukov, arXiv:1310.3455 (2013)
75. B.B. Abelev et al., Eur. Phys. J. C **73**, 2662 (2013). doi:10.1140/epjc/s10052-013-2662-9

The ALICE Collaboration

B. Abelev[69], J. Adam[37], D. Adamová[77], M. M. Aggarwal[81], M. Agnello[88,105], A. Agostinelli[26], N. Agrawal[44], Z. Ahammed[124], N. Ahmad[18], I. Ahmed[15], S. U. Ahn[62], S. A. Ahn[62], I. Aimo[88,105], S. Aiola[129], M. Ajaz[15], A. Akindinov[53], S. N. Alam[124], D. Aleksandrov[94], B. Alessandro[105], D. Alexandre[96], A. Alici[12,99], A. Alkin[3], J. Alme[35], T. Alt[39], S. Altinpinar[17], I. Altsybeev[123], C. Alves Garcia Prado[113], C. Andrei[72], A. Andronic[91], V. Anguelov[87], J. Anielski[49], T. Antičić[92], F. Antinori[102], P. Antonioli[99], L. Aphecetche[107], H. Appelshäuser[48], S. Arcelli[26], N. Armesto[16], R. Arnaldi[105], T. Aronsson[129], I. C. Arsene[91], M. Arslandok[48], A. Augustinus[34], R. Averbeck[91], T. C. Awes[78], M. D. Azmi[83], M. Bach[39], A. Badalà[101], Y. W. Baek[40,64], S. Bagnasco[105], R. Bailhache[48], R. Bala[84], A. Baldisseri[14], F. Baltasar Dos Santos Pedrosa[34], R. C. Baral[56], R. Barbera[27], F. Barile[31], G. G. Barnaföldi[128], L. S. Barnby[96], V. Barret[64], J. Bartke[110], M. Basile[26], N. Bastid[64], S. Basu[124], B. Bathen[49], G. Batigne[107], B. Batyunya[61], P. C. Batzing[21], C. Baumann[48], I. G. Bearden[74], H. Beck[48], C. Bedda[88], N. K. Behera[44], I. Belikov[50], F. Bellini[26], R. Bellwied[115], E. Belmont-Moreno[59], R. Belmont III[127], V. Belyaev[70], G. Bencedi[128], S. Beole[25], I. Berceanu[72], A. Bercuci[72], Y. Berdnikov[79,b], D. Berenyi[128], M. E. Berger[86], R. A. Bertens[52], D. Berzano[25], L. Betev[34], A. Bhasin[84], I. R. Bhat[84], A. K. Bhati[81], B. Bhattacharjee[41], J. Bhom[120], L. Bianchi[25], N. Bianchi[66], C. Bianchin[52], J. Bielčík[37], J. Bielčíková[77], A. Bilandzic[74], S. Bjelogrlic[52], F. Blanco[10], D. Blau[94], C. Blume[48], F. Bock[68,87], A. Bogdanov[70], H. Bøggild[74], M. Bogolyubsky[106], F. V. Böhmer[86], L. Boldizsár[128], M. Bombara[38], J. Book[48], H. Borel[14], A. Borissov[90,127], F. Bossú[60], M. Botje[75], E. Botta[25], S. Böttger[47], P. Braun-Munzinger[91], M. Bregant[113], T. Breitner[47], T. A. Broker[48], T. A. Browning[89], M. Broz[37], E. Bruna[105], G. E. Bruno[31], D. Budnikov[93], H. Buesching[48], S. Bufalino[105], P. Buncic[34], O. Busch[87], Z. Buthelezi[60], D. Caffarri[28], X. Cai[7], H. Caines[129], L. Calero Diaz[66], A. Caliva[52], E. Calvo Villar[97], P. Camerini[24], F. Carena[34], W. Carena[34], J. Castillo Castellanos[14], E. A. R. Casula[23], V. Catanescu[72], C. Cavicchioli[34], C. Ceballos Sanchez[9], J. Cepila[37], P. Cerello[105], B. Chang[116], S. Chapeland[34], J. L. Charvet[14], S. Chattopadhyay[124], S. Chattopadhyay[95], V. Chelnokov[3], M. Cherney[80], C. Cheshkov[122], B. Cheynis[122], V. Chibante Barroso[34], D. D. Chinellato[115], P. Chochula[34], M. Chojnacki[74], S. Choudhury[124], P. Christakoglou[75], C. H. Christensen[74], P. Christiansen[32], T. Chujo[120], S. U. Chung[90], C. Cicalo[100], L. Cifarelli[12,26], F. Cindolo[99], J. Cleymans[83], F. Colamaria[31], D. Colella[31], A. Collu[23], M. Colocci[26], G. Conesa Balbastre[65], Z. Conesa del Valle[46], M. E. Connors[129], J. G. Contreras[11], T. M. Cormier[127], Y. Corrales Morales[25], P. Cortese[30], I. Cortés Maldonado[2], M. R. Cosentino[113], F. Costa[34], P. Crochet[64], R. Cruz Albino[11], E. Cuautle[58], L. Cunqueiro[66], A. Dainese[102], R. Dang[7], A. Danu[57], D. Das[95], I. Das[46], K. Das[95], S. Das[4], A. Dash[114], S. Dash[44], S. De[124], H. Delagrange[107,a], A. Deloff[71], E. Dénes[128], G. D'Erasmo[31], A. De Caro[12,29], G. de Cataldo[98], J. de Cuveland[39], A. De Falco[23], D. De Gruttola[12,29], N. De Marco[105], S. De Pasquale[29], R. de Rooij[52], M. A. Diaz Corchero[10], T. Dietel[49], P. Dillenseger[48], R. Divià[34], D. Di Bari[31], S. Di Liberto[103], A. Di Mauro[34], P. Di Nezza[66], Ø. Djuvsland[17], A. Dobrin[52], T. Dobrowolski[71], D. Domenicis Gimenez[113], B. Dönigus[48], O. Dordic[21], S. Dørheim[86], A. K. Dubey[124], A. Dubla[52], L. Ducroux[122], P. Dupieux[64], A. K. Dutta Majumdar[95], T. E. Hilden[42], R. J. Ehlers[129], D. Elia[98], H. Engel[47], B. Erazmus[34,107], H. A. Erdal[35], D. Eschweiler[39], B. Espagnon[46], M. Esposito[34], M. Estienne[107], S. Esumi[120], D. Evans[96], S. Evdokimov[106], D. Fabris[102], J. Faivre[65], D. Falchieri[26], A. Fantoni[66], M. Fasel[87], D. Fehlker[17], L. Feldkamp[49], D. Felea[57], A. Feliciello[105], G. Feofilov[123], J. Ferencei[77], A. Fernández Téllez[2], E. G. Ferreiro[16], A. Ferretti[25], A. Festanti[28], J. Figiel[110], M. A. S. Figueredo[117], S. Filchagin[93], D. Finogeev[51], F. M. Fionda[31], E. M. Fiore[31],

E. Floratos[82], M. Floris[34], S. Foertsch[60], P. Foka[91], S. Fokin[94], E. Fragiacomo[104], A. Francescon[28,34], U. Frankenfeld[91], U. Fuchs[34], C. Furget[65], M. Fusco Girard[29], J. J. Gaardhøje[74], M. Gagliardi[25], A. M. Gago[97], M. Gallio[25], D. R. Gangadharan[19], P. Ganoti[78], C. Garabatos[91], E. Garcia-Solis[13], C. Gargiulo[34], I. Garishvili[69], J. Gerhard[39], M. Germain[107], A. Gheata[34], M. Gheata[34,57], B. Ghidini[31], P. Ghosh[124], S. K. Ghosh[4], P. Gianotti[66], P. Giubellino[34], E. Gladysz-Dziadus[110], P. Glässel[87], A. Gomez Ramirez[47], P. González-Zamora[10], S. Gorbunov[39], L. Görlich[110], S. Gotovac[109], L. K. Graczykowski[126], A. Grelli[52], A. Grigoras[34], C. Grigoras[34], V. Grigoriev[70], A. Grigoryan[1], S. Grigoryan[61], B. Grinyov[3], N. Grion[104], J. F. Grosse-Oetringhaus[34], J.-Y. Grossiord[122], R. Grosso[34], F. Guber[51], R. Guernane[65], B. Guerzoni[26], M. Guilbaud[122], K. Gulbrandsen[74], H. Gulkanyan[1], M. Gumbo[83], T. Gunji[119], A. Gupta[84], R. Gupta[84], K. H. Khan[15], R. Haake[49], Ø. Haaland[17], C. Hadjidakis[46], M. Haiduc[57], H. Hamagaki[119], G. Hamar[128], L. D. Hanratty[96], A. Hansen[74], J. W. Harris[129], H. Hartmann[39], A. Harton[13], D. Hatzifotiadou[99], S. Hayashi[119], S. T. Heckel[48], M. Heide[49], H. Helstrup[35], A. Herghelegiu[72], G. Herrera Corral[11], B. A. Hess[33], K. F. Hetland[35], B. Hippolyte[50], J. Hladky[55], P. Hristov[34], M. Huang[17], T. J. Humanic[19], N. Hussain[41], D. Hutter[39], D. S. Hwang[20], R. Ilkaev[93], I. Ilkiv[71], M. Inaba[120], G. M. Innocenti[25], C. Ionita[34], M. Ippolitov[94], M. Irfan[18], M. Ivanov[91], V. Ivanov[79], A. Jachołkowski[27], P. M. Jacobs[68], C. Jahnke[113], H. J. Jang[62], M. A. Janik[126], P. H. S. Y. Jayarathna[115], C. Jena[28], S. Jena[115], R. T. Jimenez Bustamante[58], P. G. Jones[96], H. Jung[40], A. Jusko[96], V. Kadyshevskiy[61], S. Kalcher[39], P. Kalinak[54], A. Kalweit[34], J. Kamin[48], J. H. Kang[130], V. Kaplin[70], S. Kar[124], A. Karasu Uysal[63], O. Karavichev[51], T. Karavicheva[51], E. Karpechev[51], U. Kebschull[47], R. Keidel[131], D. L. D. Keijdener[52], M. M. Khan[18,c], P. Khan[95], S. A. Khan[124], A. Khanzadeev[79], Y. Kharlov[106], B. Kileng[35], B. Kim[130], D. W. Kim[40,62], D. J. Kim[116], J. S. Kim[40], M. Kim[40], M. Kim[130], S. Kim[20], T. Kim[130], S. Kirsch[39], I. Kisel[39], S. Kiselev[53], A. Kisiel[126], G. Kiss[128], J. L. Klay[6], J. Klein[87], C. Klein-Bösing[49], A. Kluge[34], M. L. Knichel[91], A. G. Knospe[111], C. Kobdaj[34,108], M. Kofarago[34], M. K. Köhler[91], T. Kollegger[39], A. Kolojvari[123], V. Kondratiev[123], N. Kondratyeva[70], A. Konevskikh[51], V. Kovalenko[123], M. Kowalski[110], S. Kox[65], G. Koyithatta Meethaleveedu[44], J. Kral[116], I. Králik[54], F. Kramer[48], A. Kravčáková[38], M. Krelina[37], M. Kretz[39], M. Krivda[54,96], F. Krizek[77], E. Kryshen[34], M. Krzewicki[91], V. Kučera[77], Y. Kucheriaev[94,a], T. Kugathasan[34], C. Kuhn[50], P. G. Kuijer[75], I. Kulakov[48], J. Kumar[44], P. Kurashvili[71], A. Kurepin[51], A. B. Kurepin[51], A. Kuryakin[93], S. Kushpil[77], M. J. Kweon[87], Y. Kwon[130], P. Ladron de Guevara[58], C. Lagana Fernandes[113], I. Lakomov[46], R. Langoy[125], C. Lara[47], A. Lardeux[107], A. Lattuca[25], S. L. La Pointe[52], P. La Rocca[27], R. Lea[24], L. Leardini[87], G. R. Lee[96], I. Legrand[34], J. Lehnert[48], R. C. Lemmon[76], V. Lenti[98], E. Leogrande[52], M. Leoncino[25], I. León Monzón[112], P. Lévai[128], S. Li[7,64], J. Lien[125s], R. Lietava[96], S. Lindal[21], V. Lindenstruth[39], C. Lippmann[91], M. A. Lisa[19], H. M. Ljunggren[32], D. F. Lodato[52], P. I. Loenne[17], V. R. Loggins[127], V. Loginov[70], D. Lohner[87], C. Loizides[68], X. Lopez[64], E. López Torres[9], X.-G. Lu[87], P. Luettig[48], M. Lunardon[28], G. Luparello[52], C. Luzzi[34], R. Ma[129], A. Maevskaya[51], M. Mager[34], D. P. Mahapatra[56], S. M. Mahmood[21], A. Maire[87], R. D. Majka[129], M. Malaev[79], I. Maldonado Cervantes[58], L. Malinina[61,d], D. Mal'Kevich[53], P. Malzacher[91], A. Mamonov[93], L. Manceau[105], V. Manko[94], F. Manso[64s], V. Manzari[98], M. Marchisone[25,64], J. Mareš[55], G. V. Margagliotti[24], A. Margotti[99], A. Marín[91], C. Markert[111], M. Marquard[48], I. Martashvili[118], N. A. Martin[91], P. Martinengo[34], M. I. Martínez[2], G. Martínez García[107], J. Martin Blanco[107], Y. Martynov[3], A. Mas[107], S. Masciocchi[91], M. Masera[25], A. Masoni[100], L. Massacrier[107], A. Mastroserio[31], A. Matyja[110], C. Mayer[110], J. Mazer[118], M. A. Mazzoni[103], F. Meddi[22], A. Menchaca-Rocha[59], J. Mercado Pérez[87], M. Meres[36], Y. Miake[120], K. Mikhaylov[53,61], L. Milano[34], J. Milosevic[21,e], A. Mischke[52], A. N. Mishra[45], D. Miśkowiec[91], J. Mitra[124], C. M. Mitu[57], J. Mlynarz[127], N. Mohammadi[52], B. Mohanty[73,124], L. Molnar[50], L. Montaño Zetina[11], E. Montes[10], M. Morando[28], D. A. Moreira De Godoy[113], S. Moretto[28], A. Morsch[34], V. Muccifora[66], E. Mudnic[109], D. Mühlheim[49], S. Muhuri[124], M. Mukherjee[124], H. Müller[34], M. G. Munhoz[113], S. Murray[83], L. Musa[34], J. Musinsky[54], B. K. Nandi[44], R. Nania[99], E. Nappi[98], C. Nattrass[118], K. Nayak[73], T. K. Nayak[124], S. Nazarenko[93], A. Nedosekin[54], M. Nicassio[91], M. Niculescu[34,57], B. S. Nielsen[74], S. Nikolaev[94], S. Nikulin[94], V. Nikulin[79], B. S. Nilsen[80], F. Noferini[12,99], P. Nomokonov[61], G. Nooren[52], J. Norman[117], A. Nyanin[94], J. Nystrand[17], H. Oeschler[87], S. Oh[129], S. K. Oh[40,f], A. Okatan[63], L. Olah[128], J. Oleniacz[126], A. C. Oliveira Da Silva[113], J. Onderwaater[91], C. Oppedisano[105], A. Ortiz Velasquez[32], A. Oskarsson[32], J. Otwinowski[91], K. Oyama[87], P. Sahoo[45], Y. Pachmayer[87], M. Pachr[37], P. Pagano[29], G. Paić[58], F. Painke[39], C. Pajares[16], S. K. Pal[124], A. Palmeri[101], D. Pant[44], V. Papikyan[1], G. S. Pappalardo[101], P. Pareek[45], W. J. Park[91], S. Parmar[81], A. Passfeld[49], D. I. Patalakha[106], V. Paticchio[106], B. Paul[95], T. Pawlak[126], T. Peitzmann[52], H. Pereira Da Costa[14], E. Pereira De Oliveira Filho[113], D. Peresunko[94], C. E. Pérez Lara[75], A. Pesci[99], V. Peskov[48], Y. Pestov[5], V. Petráček[37], M. Petran[37], M. Petris[72], M. Petrovici[72], C. Petta[27], S. Piano[104], M. Pikna[36], P. Pillot[107], O. Pinazza[34,99], L. Pinsky[115], D. B. Piyarathna[115], M. Płoskoń[68], M. Planinic[92,121], J. Pluta[126], S. Pochybova[128], P. L. M. Podesta-Lerma[112], M. G. Poghosyan[34], E. H. O. Pohjoisaho[42], B. Polichtchouk[106], N. Poljak[92], A. Pop[72], S. Porteboeuf-Houssais[64], J. Porter[68], B. Potukuchi[84], S. K. Prasad[127], R. Preghenella[12,99], F. Prino[105], C. A. Pruneau[127], I. Pshenichnov[51], G. Puddu[23], P. Pujahari[127], V. Punin[93], J. Putschke[127], H. Qvigstad[21], A. Rachevski[106], S. Raha[4], J. Rak[116], A. Rakotozafindrabe[14], L. Ramello[30], R. Raniwala[85], S. Raniwala[85], S. S. Räsänen[42], B. T. Rascanu[48], D. Rathee[81], A. W. Rauf[15], V. Razazi[23], K. F. Read[118], J. S. Real[65], K. Redlich[71,g], R. J. Reed[129], A. Rehman[17], P. Reichelt[48], M. Reicher[52], F. Reidt[34], R. Renfordt[48], A. R. Reolon[66], A. Reshetin[51],

F. Rettig[39], J.-P. Revol[34], K. Reygers[87], V. Riabov[79], R. A. Ricci[67], T. Richert[32], M. Richter[21], P. Riedler[34], W. Riegler[34], F. Riggi[27], A. Rivetti[105], E. Rocco[52], M. Rodríguez Cahuantzi[2], A. Rodriguez Manso[75], K. Røed[21], E. Rogochaya[61], S. Rohni[84], D. Rohr[39], D. Röhrich[17], R. Romita[76], F. Ronchetti[66], L. Ronflette[107], P. Rosnet[64], A. Rossi[34], F. Roukoutakis[82], A. Roy[45], C. Roy[50], P. Roy[95], A. J. Rubio Montero[10], R. Rui[24], R. Russo[25], E. Ryabinkin[94], Y. Ryabov[79], A. Rybicki[110], S. Sadovsky[106], K. Šafařík[34], B. Sahlmuller[48], R. Sahoo[45], P. K. Sahu[56], J. Saini[124], S. Sakai[68], C. A. Salgado[16], J. Salzwedel[19], S. Sambyal[84], V. Samsonov[79], X. Sanchez Castro[50], F. J. Sánchez Rodríguez[112], L. Šándor[54], A. Sandoval[59], M. Sano[120], G. Santagati[27], D. Sarkar[124], E. Scapparone[99], F. Scarlassara[28], R. P. Scharenberg[89], C. Schiaua[72], R. Schicker[87], C. Schmidt[91], H. R. Schmidt[33], S. Schuchmann[48], J. Schukraft[34], M. Schulc[37], T. Schuster[129], Y. Schutz[34,107], K. Schwarz[91], K. Schweda[91], G. Scioli[26], E. Scomparin[105], R. Scott[118], G. Segato[28], J. E. Seger[80], Y. Sekiguchi[119], I. Selyuzhenkov[91], J. Seo[90], E. Serradilla[10,59], A. Sevcenco[57], A. Shabetai[107], G. Shabratova[61], R. Shahoyan[34], A. Shangaraev[106], N. Sharma[118], S. Sharma[84], K. Shigaki[43], K. Shtejer[25], Y. Sibiriak[94], S. Siddhanta[100], T. Siemiarczuk[71], D. Silvermyr[78], C. Silvestre[65], G. Simatovic[121], R. Singaraju[124], R. Singh[84], S. Singha[73,124], V. Singhal[124], B. C. Sinha[124], T. Sinha[95], B. Sitar[36], M. Sitta[30], T. B. Skaali[21], K. Skjerdal[17], M. Slupecki[116], N. Smirnov[129], R. J. M. Snellings[52], C. Søgaard[32], R. Soltz[69], J. Song[90], M. Song[130], F. Soramel[28], S. Sorensen[118], M. Spacek[37], E. Spiriti[66], I. Sputowska[110], M. Spyropoulou-Stassinaki[82], B. K. Srivastava[89], J. Stachel[87], I. Stan[57], G. Stefanek[71], M. Steinpreis[19], E. Stenlund[32], G. Steyn[60], J. H. Stiller[87], D. Stocco[107], M. Stolpovskiy[106], P. Strmen[36], A. A. P. Suaide[113], T. Sugitate[43], C. Suire[46], M. Suleymanov[15], R. Sultanov[53], M. Šumbera[77], T. Susa[92], T. J. M. Symons[68], A. Szabo[36], A. Szanto de Toledo[113], I. Szarka[36], A. Szczepankiewicz[34], M. Szymanski[126], J. Takahashi[114], M. A. Tangaro[31], J. D. Tapia Takaki[46,h], A. Tarantola Peloni[48], A. Tarazona Martinez[34], M. G. Tarzila[72], A. Tauro[34], G. Tejeda Muñoz[2], A. Telesca[34], J. Thäder[91], D. Thomas[52], R. Tieulent[122], A. R. Timmins[115], A. Toia[102], V. Trubnikov[3], W. H. Trzaska[116], T. Tsuji[119], A. Tumkin[93], R. Turrisi[102], T. S. Tveter[21], K. Ullaland[17], A. Uras[122], G. L. Usai[23], M. Vajzer[77], M. Vala[54,61], L. Valencia Palomo[64], S. Vallero[87], P. Vande Vyvre[34], J. Van Der Maarel[52], J. W. Van Hoorne[34], M. van Leeuwen[52], A. Vargas[2], M. Vargyas[116], R. Varma[44], M. Vasileiou[82], A. Vasiliev[94], V. Vechernin[123], M. Veldhoen[52], A. Velure[17], M. Venaruzzo[24,67], E. Vercellin[25], S. Vergara Limón[2], R. Vernet[8], M. Verweij[127], L. Vickovic[109], G. Viesti[28], J. Viinikainen[116], Z. Vilakazi[60], O. Villalobos Baillie[96], A. Vinogradov[94], L. Vinogradov[123], Y. Vinogradov[93], T. Virgili[29], Y. P. Viyogi[124], A. Vodopyanov[61], M. A. Völkl[87], K. Voloshin[53], S. A. Voloshin[127], G. Volpe[34], B. von Haller[34], I. Vorobyev[123], D. Vranic[34,91], J. Vrláková[38], B. Vulpescu[64], A. Vyushin[93], B. Wagner[17], J. Wagner[91], V. Wagner[37], M. Wang[7,107], Y. Wang[87], D. Watanabe[120], M. Weber[115], J. P. Wessels[49], U. Westerhoff[49], J. Wiechula[33], J. Wikne[21], M. Wilde[49], G. Wilk[71], J. Wilkinson[87], M. C. S. Williams[99], B. Windelband[87], M. Winn[87], C. G. Yaldo[127], Y. Yamaguchi[119], H. Yang[52], P. Yang[7], S. Yang[17], S. Yano[43], S. Yasnopolskiy[94], J. Yi[90], Z. Yin[7], I.-K. Yoo[90], I. Yushmanov[94], V. Zaccolo[74], C. Zach[37], A. Zaman[15], C. Zampolli[99], S. Zaporozhets[61], A. Zarochentsev[123], P. Závada[55], N. Zaviyalov[93], H. Zbroszczyk[126], I. S. Zgura[57], M. Zhalov[79], H. Zhang[7], X. Zhang[7,68], Y. Zhang[7], C. Zhao[21], N. Zhigareva[53], D. Zhou[7], F. Zhou[7], Y. Zhou[52], Zhou Zhuo[17], H. Zhu[7], J. Zhu[7], X. Zhu[7], A. Zichichi[12,26], A. Zimmermann[87], M. B. Zimmermann[34,49], G. Zinovjev[3], Y. Zoccarato[122], M. Zyzak[48]

[1] A.I. Alikhanyan National Science Laboratory (Yerevan Physics Institute) Foundation, Yerevan, Armenia
[2] Benemérita Universidad Autónoma de Puebla, Puebla, Mexico
[3] Bogolyubov Institute for Theoretical Physics, Kiev, Ukraine
[4] Department of Physics and Centre for Astroparticle Physics and Space Science (CAPSS), Bose Institute, Kolkata, India
[5] Budker Institute for Nuclear Physics, Novosibirsk, Russia
[6] California Polytechnic State University, San Luis Obispo, CA, USA
[7] Central China Normal University, Wuhan, China
[8] Centre de Calcul de l'IN2P3, Villeurbanne, France
[9] Centro de Aplicaciones Tecnológicas y Desarrollo Nuclear (CEADEN), Havana, Cuba
[10] Centro de Investigaciones Energéticas Medioambientales y Tecnológicas (CIEMAT), Madrid, Spain
[11] Centro de Investigación y de Estudios Avanzados (CINVESTAV), Mexico City and Mérida, Mexico
[12] Centro Fermi-Museo Storico della Fisica e Centro Studi e Ricerche "Enrico Fermi", Rome, Italy
[13] Chicago State University, Chicago, USA
[14] Commissariat à l'Energie Atomique, IRFU, Saclay, France
[15] COMSATS Institute of Information Technology (CIIT), Islamabad, Pakistan
[16] Departamento de Física de Partículas and IGFAE, Universidad de Santiago de Compostela, Santiago de Compostela, Spain
[17] Department of Physics and Technology, University of Bergen, Bergen, Norway
[18] Department of Physics, Aligarh Muslim University, Aligarh, India
[19] Department of Physics, Ohio State University, Columbus, OH, USA

[20] Department of Physics, Sejong University, Seoul, South Korea
[21] Department of Physics, University of Oslo, Oslo, Norway
[22] Dipartimento di Fisica dell'Università 'La Sapienza' and Sezione INFN, Rome, Italy
[23] Dipartimento di Fisica dell'Università and Sezione INFN, Cagliari, Italy
[24] Dipartimento di Fisica dell'Università and Sezione INFN, Trieste, Italy
[25] Dipartimento di Fisica dell'Università and Sezione INFN, Turin, Italy
[26] Dipartimento di Fisica e Astronomia dell'Università and Sezione INFN, Bologna, Italy
[27] Dipartimento di Fisica e Astronomia dell'Università and Sezione INFN, Catania, Italy
[28] Dipartimento di Fisica e Astronomia dell'Università and Sezione INFN, Padua, Italy
[29] Dipartimento di Fisica 'E.R. Caianiello' dell'Università and Gruppo Collegato INFN, Salerno, Italy
[30] Dipartimento di Scienze e Innovazione Tecnologica dell'Università del Piemonte Orientale and Gruppo Collegato INFN, Alessandria, Italy
[31] Dipartimento Interateneo di Fisica 'M. Merlin' and Sezione INFN, Bari, Italy
[32] Division of Experimental High Energy Physics, University of Lund, Lund, Sweden
[33] Eberhard Karls Universität Tübingen, Tübingen, Germany
[34] European Organization for Nuclear Research (CERN), Geneva, Switzerland
[35] Faculty of Engineering, Bergen University College, Bergen, Norway
[36] Faculty of Mathematics, Physics and Informatics, Comenius University, Bratislava, Slovakia
[37] Faculty of Nuclear Sciences and Physical Engineering, Czech Technical University in Prague, Prague, Czech Republic
[38] Faculty of Science, P.J. Šafárik University, Kosice, Slovakia
[39] Frankfurt Institute for Advanced Studies, Johann Wolfgang Goethe-Universität Frankfurt, Frankfurt, Germany
[40] Gangneung-Wonju National University, Gangneung, South Korea
[41] Department of Physics, Gauhati University, Guwahati, India
[42] Helsinki Institute of Physics (HIP), Helsinki, Finland
[43] Hiroshima University, Hiroshima, Japan
[44] Indian Institute of Technology Bombay (IIT), Mumbai, India
[45] Indian Institute of Technology Indore (IITI), Indore, India
[46] Institut de Physique Nucléaire d'Orsay (IPNO), Université Paris-Sud, CNRS-IN2P3, Orsay, France
[47] Institut für Informatik, Johann Wolfgang Goethe-Universität Frankfurt, Frankfurt, Germany
[48] Institut für Kernphysik, Johann Wolfgang Goethe-Universität Frankfurt, Frankfurt, Germany
[49] Institut für Kernphysik, Westfälische Wilhelms-Universität Münster, Münster, Germany
[50] Institut Pluridisciplinaire Hubert Curien (IPHC), Université de Strasbourg, CNRS-IN2P3, Strasbourg, France
[51] Institute for Nuclear Research, Academy of Sciences, Moscow, Russia
[52] Institute for Subatomic Physics of Utrecht University, Utrecht, The Netherlands
[53] Institute for Theoretical and Experimental Physics, Moscow, Russia
[54] Institute of Experimental Physics, Slovak Academy of Sciences, Kosice, Slovakia
[55] Institute of Physics, Academy of Sciences of the Czech Republic, Prague, Czech Republic
[56] Institute of Physics, Bhubaneswar, India
[57] Institute of Space Science (ISS), Bucharest, Romania
[58] Instituto de Ciencias Nucleares, Universidad Nacional Autónoma de México, Mexico City, Mexico
[59] Instituto de Física, Universidad Nacional Autónoma de México, Mexico City, Mexico
[60] iThemba LABS, National Research Foundation, Somerset West, South Africa
[61] Joint Institute for Nuclear Research (JINR), Dubna, Russia
[62] Korea Institute of Science and Technology Information, Taejeon, South Korea
[63] KTO Karatay University, Konya, Turkey
[64] Laboratoire de Physique Corpusculaire (LPC), Clermont Université, Université Blaise Pascal, CNRS-IN2P3, Clermont-Ferrand, France
[65] Laboratoire de Physique Subatomique et de Cosmologie, Université Grenoble-Alpes, CNRS-IN2P3, Grenoble, France
[66] Laboratori Nazionali di Frascati, INFN, Frascati, Italy
[67] Laboratori Nazionali di Legnaro, INFN, Legnaro, Italy
[68] Lawrence Berkeley National Laboratory, Berkeley, CA, USA
[69] Lawrence Livermore National Laboratory, Livermore, CA, USA
[70] Moscow Engineering Physics Institute, Moscow, Russia

[71] National Centre for Nuclear Studies, Warsaw, Poland
[72] National Institute for Physics and Nuclear Engineering, Bucharest, Romania
[73] National Institute of Science Education and Research, Bhubaneswar, India
[74] Niels Bohr Institute, University of Copenhagen, Copenhagen, Denmark
[75] Nikhef, National Institute for Subatomic Physics, Amsterdam, The Netherlands
[76] Nuclear Physics Group, STFC Daresbury Laboratory, Daresbury, UK
[77] Nuclear Physics Institute, Academy of Sciences of the Czech Republic, Řežu Prahy, Czech Republic
[78] Oak Ridge National Laboratory, Oak Ridge, TN, USA
[79] Petersburg Nuclear Physics Institute, Gatchina, Russia
[80] Physics Department, Creighton University, Omaha, NE, USA
[81] Physics Department, Panjab University, Chandigarh, India
[82] Physics Department, University of Athens, Athens, Greece
[83] Physics Department, University of Cape Town, Cape Town, South Africa
[84] Physics Department, University of Jammu, Jammu, India
[85] Physics Department, University of Rajasthan, Jaipur, India
[86] Physik Department, Technische Universität München, Munich, Germany
[87] Physikalisches Institut, Ruprecht-Karls-Universität Heidelberg, Heidelberg, Germany
[88] Politecnico di Torino, Turin, Italy
[89] Purdue University, West Lafayette, IN, USA
[90] Pusan National University, Pusan, South Korea
[91] Research Division and ExtreMe Matter Institute EMMI, GSI Helmholtzzentrum für Schwerionenforschung, Darmstadt, Germany
[92] Rudjer Bošković Institute, Zagreb, Croatia
[93] Russian Federal Nuclear Center (VNIIEF), Sarov, Russia
[94] Russian Research Centre Kurchatov Institute, Moscow, Russia
[95] Saha Institute of Nuclear Physics, Kolkata, India
[96] School of Physics and Astronomy, University of Birmingham, Birmingham, UK
[97] Sección Física, Departamento de Ciencias, Pontificia Universidad Católica del Perú, Lima, Peru
[98] Sezione INFN, Bari, Italy
[99] Sezione INFN, Bologna, Italy
[100] Sezione INFN, Cagliari, Italy
[101] Sezione INFN, Catania, Italy
[102] Sezione INFN, Padua, Italy
[103] Sezione INFN, Rome, Italy
[104] Sezione INFN, Trieste, Italy
[105] Sezione INFN, Turin, Italy
[106] SSC IHEP of NRC Kurchatov institute, Protvino, Russia
[107] SUBATECH, Ecole des Mines de Nantes, Université de Nantes, CNRS-IN2P3, Nantes, France
[108] Suranaree University of Technology, Nakhon Ratchasima, Thailand
[109] Technical University of Split FESB, Split, Croatia
[110] The Henryk Niewodniczanski Institute of Nuclear Physics, Polish Academy of Sciences, Kracòw, Poland
[111] Physics Department, The University of Texas at Austin, Austin, TX, USA
[112] Universidad Autónoma de Sinaloa, Culiacán, Mexico
[113] Universidade de São Paulo (USP), São Paulo, Brazil
[114] Universidade Estadual de Campinas (UNICAMP), Campinas, Brazil
[115] University of Houston, Houston, TX, USA
[116] University of Jyväskylä, Jyväskylä, Finland
[117] University of Liverpool, Liverpool, UK
[118] University of Tennessee, Knoxville, TN, USA
[119] University of Tokyo, Tokyo, Japan
[120] University of Tsukuba, Tsukuba, Japan
[121] University of Zagreb, Zagreb, Croatia
[122] Université de Lyon, Université Lyon 1, CNRS/IN2P3, IPN-Lyon, Villeurbanne, France

[123] V. Fock Institute for Physics, St. Petersburg State University, St. Petersburg, Russia
[124] Variable Energy Cyclotron Centre, Kolkata, India
[125] Vestfold University College, Tonsberg, Norway
[126] Warsaw University of Technology, Warsaw, Poland
[127] Wayne State University, Detroit, MI, USA
[128] Wigner Research Centre for Physics, Hungarian Academy of Sciences, Budapest, Hungary
[129] Yale University, New Haven, CT, USA
[130] Yonsei University, Seoul, South Korea
[131] Zentrum für Technologietransfer und Telekommunikation (ZTT), Fachhochschule Worms, Worms, Germany

[a] Deceased
[b] Also at: St. Petersburg State Polytechnical University, St. Petersburg, Russia
[c] Also at: Department of Applied Physics, Aligarh Muslim University, Aligarh, India
[d] Also at: M.V. Lomonosov Moscow State University, D.V. Skobeltsyn Institute of Nuclear Physics, Moscow, Russia
[e] Also at: University of Belgrade, Faculty of Physics and "Vinča" Institute of Nuclear Sciences, Belgrade, Serbia
[f] *Permanent Address*: Konkuk University, Seoul, Korea
[g] Also at: Institute of Theoretical Physics, University of Wroclaw, Wrocław, Poland
[h] Also at: University of Kansas, Lawrence, KS, USA